A Prognostic Parameterization for the Subgrid-Scale Variability of Water Vapor and Clouds in Large-Scale Models and Its Use to Diagnose Cloud Cover

Adrian M. Tompkins[*]

Max-Planck-Institut für Meteorologie, Hamburg, Germany

ABSTRACT

A parameterization for the horizontal subgrid-scale variability of water vapor and cloud condensate is introduced, which is used to diagnose cloud fraction in the spirit of statistically based cloud cover parameterizations. High-resolution cloud-resolving model data from tropical deep convective scenarios were used to justify the choice of probability density function (PDF). The PDF selected has the advantage of being bounded above and below, avoiding the complications of negative or infinite water mixing ratios, and can give both negatively and positively skewed functions as well as symmetric Gaussian-like bell-shaped curves, without discrete transitions, and is mathematically straightforward to implement.

A development from previous statistical parameterizations is that the new scheme is prognostic, with processes such as deep convection, turbulence, and microphysics directly affecting the distribution of higher-order moments of variance and skewness. The scheme is able to represent the growth and decay of cirrus cloud decks and also the creation of cloud in clear sky or breakup of an overcast cloud deck by boundary layer turbulence. After introducing the mathematical framework, results using the parameterization in a climate model are shown to illustrate its behavior. The parameterization is shown to reduce cloud cover biases almost globally, with a marked improvement in the stratocumulus regions in the eastern Pacific and Atlantic Oceans.

1. Introduction

Since clouds have a significant influence on the global hydrological and thermodynamic budgets, the inclusion of cloud processes in global climate and forecast models is an important task. This is complicated by the fact that clouds are not resolved at the current resolutions used by general circulation models (GCMs), and therefore must be parameterized.

The art of cloud parameterization appears to have evolved steadily in complexity since early models fixed cloud properties to observed values. Current schemes often use prognostic equations for predicting various cloud and precipitation variables, such as cloud ice, rain, or snow, and include parameterizations of a large number of microphysical pathways between these categories (e.g., Lohmann and Roeckner 1996; Fowler et al. 1996; Ghan et al. 1997). Many schemes are of comparable complexity to those used in cloud-resolving model (CRM) studies (e.g., Lin et al. 1983; Brown and Swann 1997). However, since CRMs claim, by definition, to resolve cloud-scale motions, they usually adopt a simple assumption concerning the fractional cloud cover in each grid cell, assuming total cover if any significant amount of cloud condensate is present. Although some GCM cloud schemes also use a similar approach, (Ose 1993; Fowler et al. 1996), this ''binary'' assumption of total or zero cloud cover is clearly not adequate with the horizontal resolution used by global-scale models.

The ''all-or-nothing'' parameterization of cloud cover used by CRMs essentially assumes that no subgrid-scale variability of water variables exists. Fractional cloudiness is the result of subgrid-scale variability, and a group of schemes commonly in use attempt to represent this by relating cloud cover to relative humidity (RH) (e.g., Sellers 1976; Gates and Schlesinger 1977; Schneider et al. 1978; Sundqvist 1978; Slingo 1980; Sundqvist et al. 1989; Walcek 1994; Lohmann and Roeckner 1996; DelGenio et al. 1996), with cloud cover increasing monotonically from zero at some critical RH according to a specified function. It is straightforward to see that the critical RH at which cloud forms is therefore a measure of the subgrid-scale variability that is assumed to exist. Some schemes also take other factors such as vertical velocity into account (e.g., Slingo 1987).

A second group of schemes are sometimes referred to as ''statistical schemes.'' These schemes, stemming from the work of Sommeria and Deardorff (1977), Mellor (1977), and Bougeault (1981), assign a probability

---

* Current affiliation: ECMWF, Shinfield Park, Reading, United Kingdom.

Corresponding author address: Dr. Adrian M. Tompkins, ECMWF, Shinfield Park, Reading, Berkshire RG2 9AX, United Kingdom.
E-mail: Tompkins@ecmwf.int

density function (PDF) to the total water mixing ratio (r_t)[1] equal to the sum of the water vapor, cloud water, and cloud ice mixing ratios. If the statistical moments of the distribution of r_t are known, then the cloud fraction can be diagnosed by simply integrating the super-saturated part of the PDF. The difficult task of these schemes is the specification of an appropriate (and mathematically tractable) PDF for r_t, and the determination of its moments such as the variance. Various distributions have been attempted, many of which are symmetrical. Smith (1990) uses a symmetric triangular PDF, diagnosing the variance based on a critical RH function at which cloud is determined to form, later modified by Cusack et al. (1999). This PDF has been subsequently adopted by Rotstayn (1997) and Nishizawa (2000). LeTreut and Li (1991) use a uniform distribution, setting the distribution's variance to an arbitrarily defined constant. A Gaussian-like symmetrical polynomial function was used by Lohmann et al. (1999) with variance determined from the subgrid-scale turbulence scheme following Ricard and Royer (1993), who investigated Gaussian, exponential, and skewed PDF forms. Bechtold et al. (1992) based their scheme on the Gaussian distribution, which was modified in Bechtold et al. (1995) to a PDF linearly interpolated between Gaussian and exponential distributions. Lewellen and Yoh (1993) detail a parameterization that uses a binormal distribution that can be skewed as well as symmetrical and is bimodal, although a number of simplifying assumptions were necessary in order to make the scheme tractable.

It is important to stress that there is not a clear distinction between the so-called RH schemes and statistical schemes. If a time-invariant variance is used in a statistical scheme, it can be reduced to an RH-type formulation. The RH scheme of Sundqvist (1978) can be derived by assuming a uniform distribution for total water, for instance, and Smith (1990) gives the equivalent RH formulation for the triangular distribution used in that scheme. Parameterizations such as Xu and Randall (1996a), who relate cloud fraction to RH and cloud condensate, can be viewed as manifestations of a statistical scheme where the actual PDF of total water is itself not known, but the time-mean statistics of its integral are.

If the variance (and/or higher-order moments) are allowed to vary in a statistical scheme, these schemes can provide a more realistic link between clouds and other physical processes. For example, an undisturbed planetary boundary layer (PBL) may become partly cloudy when turbulence occurs, due to the increase of the subgrid-scale variability. An additional advantage that statistical schemes have is that, since the PDF of water vapor and cloud is known, the information can also be

used in other model components, increasing the self-consistency of the model. For example, the information concerning the subgrid variability of clouds can be used for a more accurate calculation of radiative fluxes. Cahalan et al. (1994), Barker et al. (1999), Pincus et al. (1999), Pomroy and Illingworth (2000), and Fu et al. (2000) have showed, in various observational and modeling studies, how representing the variability of water and cloud is crucial for accurate calculation of radiative fluxes for a large variety of cloud situations, and Barker (1996), Oreopoulos and Barker (1999), and Cairns et al. (2000) have attempted to include parameterizations for these effects in GCM radiative calculations. Tiedtke (1996), for example, showed that taking into account cloud inhomogeneities led to more realistic shortwave radiative fluxes. Since the information concerning cloud variability is not generally available in most current GCMs, effectively hidden in such parameters as the critical RH for cloud formation, radiative parameterizations make their own independent estimate, often unaffected by the dynamical situation. It would be much more desirable to use a consistent estimate of variability in the calculation of cloud fraction and radiative fluxes, thus reducing the total number of model "tunable" parameters. Knowing the inhomogeneity of clouds also permits a more accurate derivation of microphysical processes such as precipitation formation, which are highly nonlinear, resulting in potentially substantial biases if the grid mean value is used (Pincus and Klein 2000; Rotstayn 2000; Larson et al. 2001b).

From the brief review of statistical schemes it is apparent that a widely varying selection of PDFs have been used. One reason for this is that it is difficult to obtain generalized and accurate information from observations concerning variability down to small scales, as noted by Lohmann et al. (1999), forcing the decision concerning the function form to be somewhat ad hoc. Previous observational studies have included measurements by aircraft (Ek and Mahrt 1991; Wood and Field 2000; Davis et al. 1996; Larson et al. 2001a), tethered balloon (Price 2001), and satellite instrumentation (Wielicki and Parker 1994; Barker et al. 1996). However, each of these data sources suffers from various drawbacks. For example, aircraft or tethered balloon data usually only provide a one-dimensional (1D) path through a cloud field, possibly leading to undersampling problems. Measured bi- or multimodel distributions could be absent or less prominent if 2D horizontal slices containing an ensemble of clouds could be simultaneously analyzed. On the other hand currently available satellite data have difficulties vertically resolving water vapor and/or cloud structure. It is therefore apparent that CRMs (where the term is used in a broad sense and includes large eddy simulations) can offer a complementary tool to observations, enabling analysis of fully 3D-simulated cloud fields. Bougeault (1982) pioneered this use of a CRM, using the simulations of Sommeria (1976). Other authors to use models in this way include

---

[1] Usually temperature variability, which affects the local saturation vapor pressure, is also taken into account, but we refer here to r_t for simplicity.

Lewellen and Yoh (1993), Xu and Krueger (1991), and Xu and Randall (1996a), for example. The first aim of this paper therefore, is to use a 3D CRM, on domains on the order of a climate model grid box but also with relatively high horizontal resolution, to assess whether a generalized function form exists that can describe the total water variability. For this initial study, a tropical scenario is used, since it is assumed that situations where deep convection is introducing large localized perturbations in the water vapor field will be the most difficult to represent.

The second aspect that is uncertain with statistical schemes is the determination of the distribution moments. For example, Lohmann et al. (1999) follow Ricard and Royer (1993) by using the turbulent activity to determine the distribution variance, setting a constant minimum variance that usually operated above the turbulent PBL. However, the variance of water substance will also be affected by other physical processes not taken into account: gravity wave activity, subgrid-scale horizontal eddy mixing, and probably most importantly, deep convective activity. Unlike PBL turbulence, some of these processes act on timescales much longer than a GCM time step (e.g., convectively generated cirrus anvil dissipation), implying that a prognostic scheme is more appropriate. Tiedtke (1993) and Mannoji (1995) have previously developed schemes that treat cloud cover itself directly as a prognostic parameter. As discussed by Wang and Wang (1999), such a scheme can be developed consistently with the statistical approach by converting time changes of distribution properties into source or sink terms for cloud cover. Indeed, some of the prognostic terms for cloud cover in the Tiedtke (1993) scheme, such as the creation of cloud by adiabatic or diabatic cooling, are derived directly using assumptions concerning the subgrid-scale distribution of total water. However, this is accomplished on a term-by-term basis, and without the framework of a statistically based scheme can lead to inconsistent cloud cover predictions with regard to the cloud condensate and water vapor quantities.

The scheme introduced in this paper attempts to incorporate processes such as deep convection into a prognostic implementation of a statistical scheme. After briefly introducing the statistical cloud scheme framework in section 2, section 3 analyzes the CRM data to identify a suitable PDF form to use. Section 4 describes the framework for the new prognostic scheme, while the following section describes how convection and other processes affect the higher-order PDF moments of variance and skewness. Results from the implementation of the scheme in a GCM are given in section 6.

2. Statistical cloud schemes

The basis of statistical cloud schemes is summarized; Bougeault (1981), Smith (1990), Xu and Randall (1996b), and Lohmann et al. (1999) provide greater de-

tail. Since water vapor perturbations can be correlated with temperature perturbations, which alter the local saturation vapor pressure, it has been useful to form a variable s, defined as

$$s = a_l(r_t' - \alpha_l T_l'), \qquad (1)$$

where r_t' is the fluctuation of the total water mixing ratio r_t equal to the sum of the vapor (r_v), cloud ice (r_i), and liquid cloud water (r_l) mixing ratios, and T_l' is the liquid water temperature fluctuation. The fluctuations are defined about the mean thermodynamic state $\overline{T}_l$, and the constants are defined as $\alpha_l = (\partial r_s / \partial T)(\overline{T}_l)$ and $a_l = [1 + (L/c_p)\alpha_l]^{-1}$, where r_s is the saturation vapor mixing ratio, L is the latent heat of vaporization, and c_p is the specific heat of dry air. Physically, s describes the distance between the thermodynamic state to the linearized saturation vapor mixing ratio curve. Defining $s_s = a_l(r_s - \overline{r}_t)$ the cloud condensate mass r_c ($= r_l + r_i$) is given by $r_c = s - s_s$, providing $s > s_s$. Assuming that any supersaturation efficiently condenses to cloud, a common assumption in current GCM cloud schemes, it is possible to express the cloud fraction c as

$$c = \int_{s_s}^{\infty} G(s) \, ds, \qquad (2)$$

where $G(s)$ is the PDF of s. The assumption that supersaturation does not occur is a good approximation for warm clouds, but observations show that large supersaturations with respect to ice can often exist (Heymsfield and Miloshevich 1995; Heymsfield et al. 1998a,b). Relaxing this assumption for the ice phase will be the subject of future research.

The variance of s, and therefore the associated liquid water and cloud cover, depends on the correlation between T_l and r_t perturbations in addition to their respective magnitudes:

$$\sigma^2(s) = a_l^2(\overline{r_t'^2} + \alpha_l \overline{T_l'^2} - 2\alpha_l \overline{r_t' T_l'}). \qquad (3)$$

This aspect was disregarded by many previous statistical schemes, which were formulated in terms of s, but simply set the variance to a fixed or arbitrary value. In such schemes it is not known whether cloud is a result of temperature perturbations, water perturbations, or a combination of the two. Some parameterizations, such as Ricard and Royer (1993) have calculated temperature perturbations separately that result from turbulence. However, here the aim is to develop a scheme where the distribution moments are directly influenced by several cloud-generating processes prognostically. Representing the higher-order moments of temperature in addition to moisture (and their correlation) greatly increases the level of complexity and computational expense of such a scheme. Temperature fluctuations are likely to be smaller in magnitude than total water fluctuations, especially in the Tropics where gravity waves remove lateral fluctuations of virtual temperature on fast timescales (Bretherton and Smolarkiewicz 1989). Re-

cent observational data from Price and Wood (2001, submitted to *Quart J. Roy. Meteor. Soc.*) also seems to confirm that temperature fluctuations are less important than humidity fluctuations, even in the lower troposphere in midlatitudes. Therefore, this first attempt at a prognostic statistical scheme tackles the zero-order problem of representing the fluctuations of cloud and water vapor. The subgrid-scale variability of temperature is neglected, as in LeTreut and Li (1991), and r_s is assumed to be constant throughout a grid cell.

The definition of cloud cover in (2) simplifies to

$$c = \int_{r_s}^{\infty} G(r_t) \, dr_t, \qquad (4)$$

with the cloud condensate given by

$$\bar{r}_c = \int_{r_s}^{\infty} (r_t - r_s) G(r_t) \, dr_t. \qquad (5)$$

It is the goal of this paper to determine a suitable functional form for $G(r_t)$ and the way in which the unresolved processes such as turbulence and deep convection affect its variance and skewness, thereby determining the cloud cover.

3. Cloud statistics

a. Model data

In this section, an attempt is made to find a general and simple functional form that can describe the variability of r_t in cloud resolving model simulations. A brief description of the CRM and the simulation scenario used to produce the data is given in the appendix.

The statistics of r_t in the CRM are examined for individual model field "snapshots," rather than mean distributions as in Xu and Randall (1996b), since the aim is to be able to prognostically model the temporally evolving PDF, and not just its mean distribution. Figure 1 shows the PDF of r_t for various model levels throughout the troposphere, at the last time step of the experiment. Examination of the PDFs every half hour throughout the experiment proved them to be very similar in characteristics, since the computational domain was sufficient in size to continuously contain an ensemble of clouds, and the initial conditions were a realistic field of clouds in a state of quasi-equilibrium. The data at the 65 536 grid points are divided into 200 bins of equal width. At all heights the distribution is approximately "bell" shaped, and appears to be approximately unimodal, although there is some hint of bimodality at some upper-tropospheric levels. Note that the use of a sufficiently large horizontal 3D domain in conjunction with high resolution implies that convection is continuously present, with convective cores (defined by an absolute magnitude vertical velocity exceeding 1 m s^{-1}) occupying a small proportion of the domain, typically a fraction of a percent. A result of this is that the dis-

tribution of r_t at only the nonconvective grid points is virtually indistinguishable from that using the entire domain.

Considering the functions previously used in statistical schemes, it is obvious that the uniform distribution, for example, is a poor candidate for the r_t distribution. Additionally, the distribution is seen to be positively skewed throughout most of the troposphere to varying degrees, but with the PBL exhibiting negative skewness. The positive skewness is the result of convective activity that provides isolated sources of high r_t values. In the same way, the negative skewness in the PBL is the direct result of convectively generated downdrafts. Examination of all the other time periods reveal these same distribution features.

The first task is to identify a general functional form that can model these distribution characteristics. Although it is difficult to theoretically derive a PDF form, since the r_t distribution is the result of a large number of interacting processes, therefore forcing the use of empirical methods, it is possible to use physically based arguments to justify certain functional forms. For example, in the absence of other processes, large-scale dynamical mixing would tend to reduce both the variance and the asymmetry the distribution. Therefore, the gamma and lognormal distributions would be difficult to use since they are always positively skewed and only tend to a symmetrical distribution as one of their defining parameters approaches infinity.

Another problem that distributions such as the lognormal, gamma, Gaussian, and exponential suffer from is that they are all unbounded functions. Thus, if these functional forms are used, the maximum cloud condensate mixing ratio approaches infinity, and part of the grid cell is always covered by cloud. Precautionary measures, such as the use of a truncated function, can be taken, but this increases the number of parameters required to describe the distribution, and again introduces undesirable discreteness. Moreover, functions such as the Gaussian function or the polynomial used by Lohmann et al. (1999) are also negatively unbounded, implying that part of the grid cell has negative water mass. The choice of function must also involve a fair degree of pragmatism, since in addition to providing a good fit to the available data, it must also be sufficiently simple and of few enough degrees of freedom to be of use in a parameterization scheme. For example, Larson et al. (2001a) were able to provide good fits to their aircraft data using a five-parameter double Gaussian function, but it is unclear how these parameters would be determined in a GCM cloud scheme.

Considering the distribution characteristics noted above, one possible candidate is the beta distribution (Johnson and Kotz 1970; Essenwanger 1976), where the PDF $G(t)$ is defined as

$$G(t) = \frac{1}{B(p, q)} \frac{(t - a)^{p-1}(b - t)^{q-1}}{(b - a)^{p+q-1}} \qquad (a \leq t \leq b) \quad (6)$$
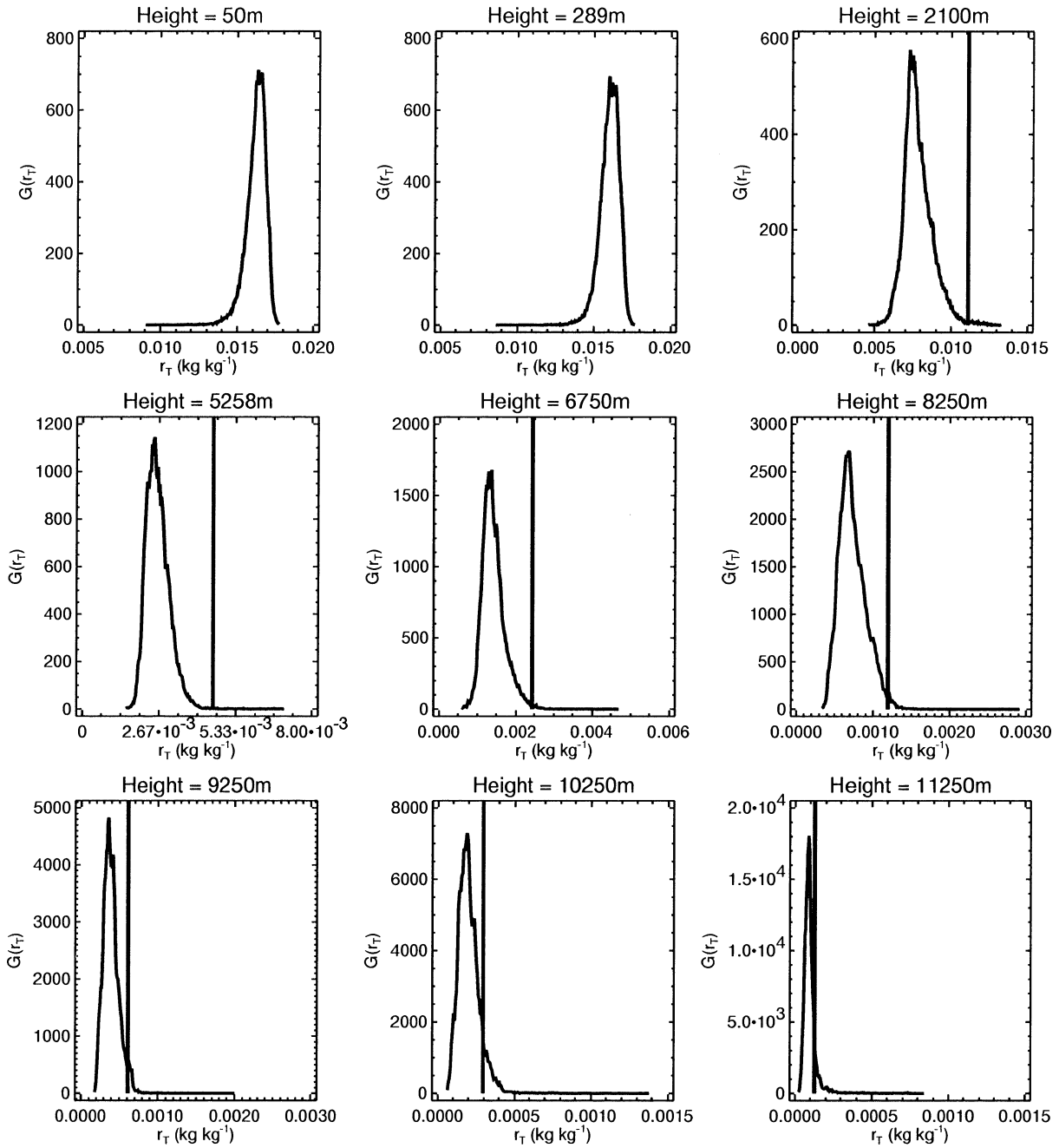
FIG. 1. PDFs of r_t taken at nine various model levels at the end of the simulation period. The vertical line represents $\overline{r}_s$, the mean of r_s calculated at each grid point.

with $p > 0$, $q > 0$. The symbol B represents the beta function, and can be defined in terms of the gamma function Γ as follows:

$$B(p, q) = \frac{\Gamma(p)\Gamma(q)}{\Gamma(p + q)}. \qquad (7)$$

The distribution is bounded by b and a and is extremely flexible, taking on J, U, or bell shapes (Johnson and Kotz 1970), although we will restrict ourselves to

the $p > 1$, $q > 1$ bell-shaped regime. Figure 2 gives some example beta curves between arbitrary limits. The skewness (ς) of the distribution is related to the difference between the two shape parameters p and q,

$$\varsigma = \frac{2(q - p)}{p + q + 2}\sqrt{\frac{p + q + 1}{pq}}, \qquad (8)$$

and thus if $p = q$ the distribution is symmetrical, but
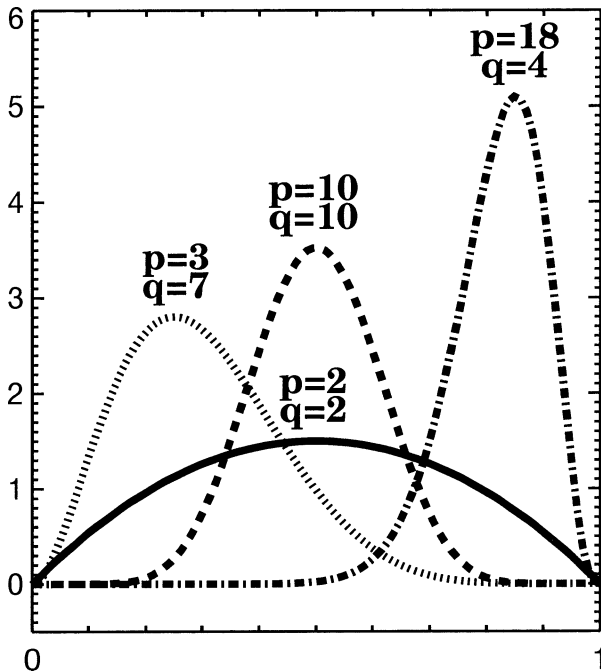
FIG. 2. Examples of the beta distribution for various combinations of the shape-defining parameters p and q.

also both positively and negatively skewed distributions are possible. As p and q tend to infinity the curve approaches the Normal distribution. The standard deviation of the distribution is given by

$$\sigma = \frac{b - a}{p + q}\sqrt{\frac{pq}{p + q + 1}} \qquad (9)$$

and thus is directly related to the distribution width $b - a$ as expected.

In addition to being bounded and also easily giving both skewed and symmetrical functions, the beta distribution has the additional advantage that it is a function of only four parameters and as will be shown later, is also mathematically straightforward to incorporate into the statistical scheme framework. In order to compare the beta function to the cloud model data, a method is required to calculate the "best-fit" curve. Three procedures are used here and in each, the minimum and maximum values of r_t from the CRM data are used directly to define the PDF bounds, a and b. As the beta function is defined by four parameters, two additional items of information are required to define the shape parameters p and q. For the first fitting method, we use the mean and variance of r_t. The resulting PDF will divide r_t correctly only between cloud and water vapor if the beta distribution renders a perfect fit to the data. A second fitting method is to use $\overline{r}_c$ (when present), instead of the variance, which enforces the correct division of total water into cloud and vapor. The third method uses cloud cover instead of variance to find

the beta distribution that gives the correct cloud cover given $\overline{r}_t$.

Examining the distributions at the nine levels (Fig. 3), it appears that at each height, a reasonable fit using the Beta distribution can be obtained. The distributions are plotted on a logarithmic scale to allow easier comparison at the distribution extremes, which also more clearly reveals evidence of secondary distribution peaks in the convective detrainment region. It should be remembered that the fit is made at one, illustrative point in time here, and the secondary distribution peak is not a time-invariant feature. Analysis of other times indicates that the distribution is often unimodal (not shown). In the PBL, the variance-fitting method produces a close match to the observed PDF. At levels where cloud is present the quality of fit varies. At 2 km, the beta distribution has too much power at the distribution extremes, and again at 5 km the presence of a secondary peak in the data causes the beta distribution to be too wide. In the convective detrainment zone above 11 km the observed distribution has more power at the large cloud-mixing ratio tail, resulting in the beta fits underestimating the number of grid points with these high cloud mixing ratios. However, the beta distribution reproduces the bulk of the distribution reasonably well.

Although specific examples can be found where some of the alternative distributions, such as the gamma or the log-normal distributions, offer better fits than the beta distribution, there are also cases where the opposite is true, and none are able to offer a general improvement on the beta distribution. Also, examination of other CRM data found sensitivity in the details of the observed distributions, such as the flatness of the distribution tails to changing the microphysical parameterization, as one would reasonably expect. However, the beta distribution was able to render the generalized characteristics of the statistical distribution in each case.

b. Observational data

One of the possible limitations of the beta distribution is that it is unimodal. A brief review of the observational literature is therefore conducted in order to assess how generally appropriate the beta distribution is for describing r_t variability, with particular regard paid to the frequency of occurrence of unimodal distributions.

Ek and Mahrt (1991) examined PBL relative humidity variability in a limited number of flight legs, and assumed a unimodal Gaussian fit for their distribution. Recently, Wood and Field (2000) studied flight data from both warm and cold clouds and reported unimodal distributions of r_t, but also observing more complex distributions, giving some weakly and strongly bimodal examples. Davis et al. (1996) reported uni- or bimodal skewed distributions in liquid water content from flight data in marine stratocumulus clouds. Larson et al. (2001a) have also examined flight data for PBL clouds and found that mainly unimodal or bimodal distributions
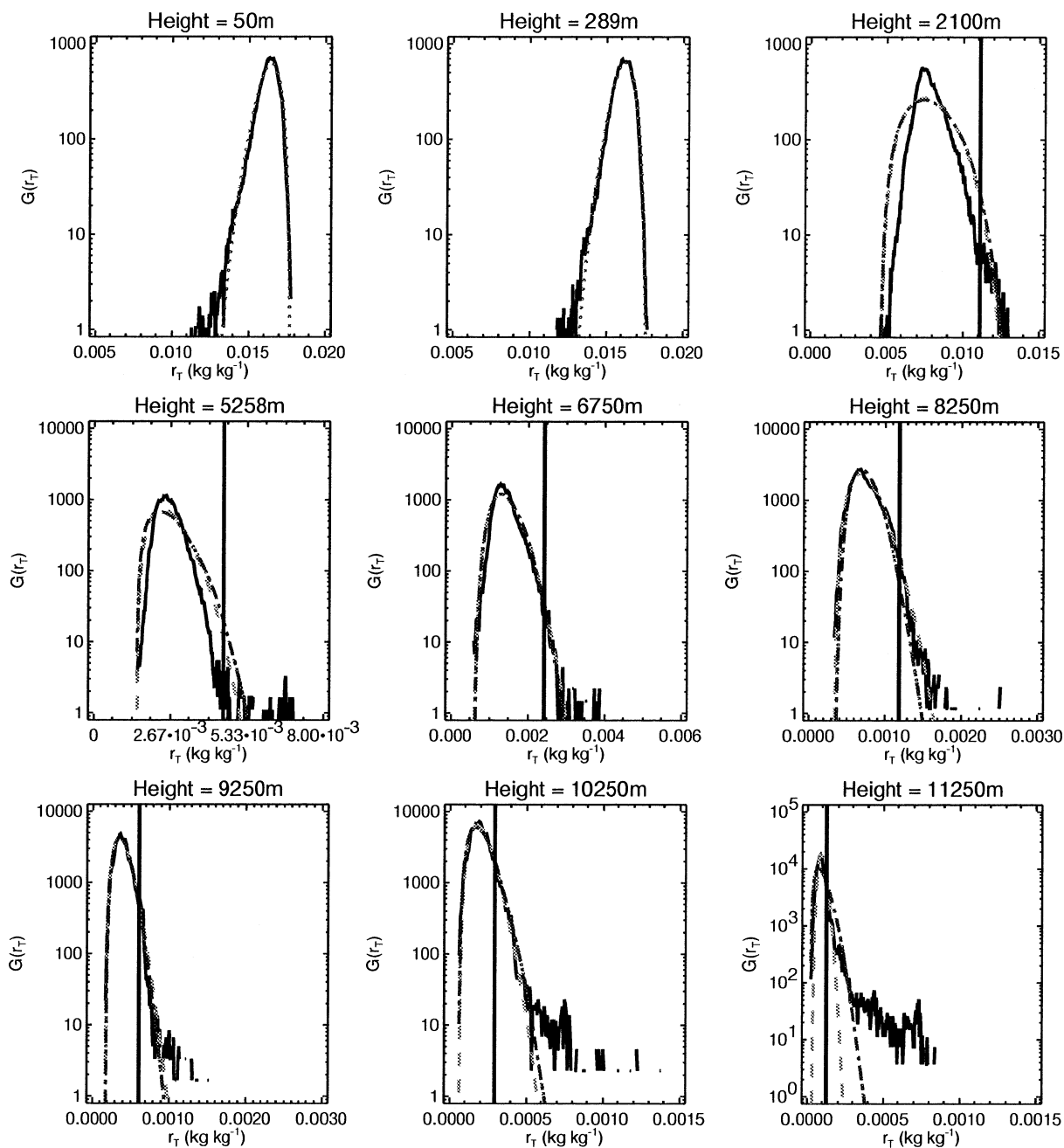
FIG. 3. As for Fig. 1 but plotted on a logarithmic scale, and with three best-fit beta distribution curves superimposed. In addition to the observed distribution limits, the dotted line uses the mean and variance of r_t, the dot–dashed line uses the mean and r_c, and the dashed line fit uses the mean and the cloud fraction (see text for details). Only the variance fit is shown in the PBL where $r_c = 0$.

occurred. They reported that PDFs that included positive or negative skewness were able to give an improved fit for the data.

Price (2001) used tethered balloon data of PBL humidity collected during a 3-yr period, finding that roughly half of the data could be classified as symmetrical or skewed unimodal. A further 25% of the data could be regarded as multimodal. Encouragingly, Price (2001) tested the suitability of a number of common symmetric

and skewed distribution forms, and found that the beta distribution produced the best fit.

Although many of the above studies reported a significant frequency of occurrence of distributions classed as bi- or multimodal, these distributions often possessed a single principal distribution peak, as in the example given by Price (2001), and thus the beta distribution could still offer a reasonable approximation to these cases. This also applies to the flight data examples

shown in Heymsfield and McFarquhar (1996) taken in ice clouds. Additionally, as stated in the introduction, the bimodal and multimodal distributions may be exaggerated in both flight and balloon data. Satellite data on the other hand can give a more global view at relatively high spatial resolutions. Two such studies have been reported by Wielicki and Parker (1994) and Barker et al. (1996), who used Landsat data at a resolution of 28.5 m to examine liquid water path in a large variety of cloud cover situations. They reported unimodal distributions in nearly or totally overcast scenes, and exponential-type distributions in scenes of low cloud fraction, as expected since in these cases only the tail of the r_t distribution is detected. A truncated gamma distribution was found to give a good approximation to the data, although it is apparent that the beta distribution could offer an improved fit for some of the observed cases with reduced power at the thickest cloud depths. Interestingly, neither study reported an example of a multimodal distribution.

In summary, it appears that in the observational data available, gathered over a wide variety of cloud conditions (although rarely in ice clouds), approximate unimodality was fairly widespread, and that a flexible skewed function such as the beta distribution can offer a reasonable approximation to the observed variability of total water. That said, future developments to include the use of a bimodal function such as that of Lewellen and Yoh (1993) may lead to improvements.

4. Cloud scheme framework

The cloud scheme assumes that the PDF describing the distribution of the total water mixing ratio r_t can always be described by a beta distribution, as given by Eq. (6). Thus $\bar{r}_t$ (where the overbar represents the grid-point mean value) is given by

$$\bar{r}_t = \frac{1}{B(p, q)} \int_a^b \frac{r_t(r_t - a)^{p-1}(b - r_t)^{q-1}}{(b - a)^{p+q-1}} \, dr_t, \quad (10)$$

where a and b represent the minimum and maximum values of r_t, respectively. It is usual to apply the coordinate transformation $y = (r_t - a)/(b - a)$, giving

$$\bar{r}_t = \frac{1}{B(p, q)} \int_0^1 [y(b - a) + a]y^{p-1}(1 - y)^{q-1} \, dy. \quad (11)$$

Using (7) and (11) in conjunction with the gamma function relationship $\Gamma(p + 1) = p\Gamma(p)$, the usual expression for the mean of a beta distribution is attained:

$$\bar{r}_t = (b - a)\frac{p}{p + q} + a. \quad (12)$$

It is straightforward to similarly gain expressions for the water vapor and cloud condensate:

$$\bar{r}_v = (b - a)\frac{p}{p + q}I_{(r_s-a)/(b-a)}(p + 1, q)$$
$$+ (a - r_s)I_{(r_s-a)/(b-a)}(p, q) + r_s, \quad (13)$$

$$\bar{r}_c = (b - a)\frac{p}{p + q}[1 - I_{(r_s-a)/(b-a)}(p + 1, q)]$$
$$+ (a - r_s)[1 - I_{(r_s-a)/(b-a)}(p, q)], \quad (14)$$

which can be combined to give (12). The incomplete beta function ratio I_x is defined as

$$I_x(p, q) = \frac{1}{B(p, q)} \int_0^x t^{p-1}(1 - t)^{q-1} \, dt, \quad (15)$$

subject to the limits $I_0(p, q) = 0$ and $I_1(p, q) = 1$.

Exactly four parameters are required to uniquely define the beta distribution. For example, one can use the distribution limits a and b, and the shape parameters p and q. Alternatively one could specify the first four moments of the distribution. The approach we will take is to introduce prognostic equations for the shape parameters p and q so that they are known at each time step. Thus two further parameters are required and for these it is possible to use $\bar{r}_t$ and $\bar{r}_c$, which are already prognosed in the model. Thus p, q, $\bar{r}_t$, and $\bar{r}_c$ uniquely define the beta distribution, and all of the distribution's other properties, such as the minimum and maximum values, a and b, and the variance and skewness can be subsequently diagnosed. This is illustrated schematically in Fig. 4. The top panel shows a variety of beta distribution PDFs, all of which have the same shape (i.e., identical p and q) and all of which have the same mean value, equal to $\bar{r}_t$. Although there are an infinite number of such curves with these properties, only one unique PDF will give the correct values for $\bar{r}_v$ and $\bar{r}_c$.

The two light PDFs illustrate the limits necessary to retain a physically reasonable solution in partially cloudy regimes. One curve illustrates the narrowest possible PDF, for which the cloud fraction and condensate mass is zero. The second case is for the widest possible PDF, for which the distribution minimum equals zero (i.e., a wider PDF would imply negative water amounts in some parts of the grid cell). As the PDF is progressively widened from the narrowest extreme upward, the corresponding cloud-mixing ratio increases monotonically from zero to its maximum value (for which $a = 0$). This is illustrated in the lower panel of the figure. To determine the exact PDF that gives $\bar{r}_c$ (the dark curve), (12) is substituted into (13) to give an iterable function for a, thus:

$$(\bar{r}_t - a)I_{r_s'}(p + 1, q) + (a - r_s)I_{r_s'}(p, q)$$
$$+ r_s - \bar{r}_v = 0, \quad (16)$$

where $r_s' = p(r_s - a)(\bar{r}_t - a)^{-1}(p + q)^{-1}$.

Since this function is monotonic it can be quickly and robustly solved by any simple iteration method (see ap-
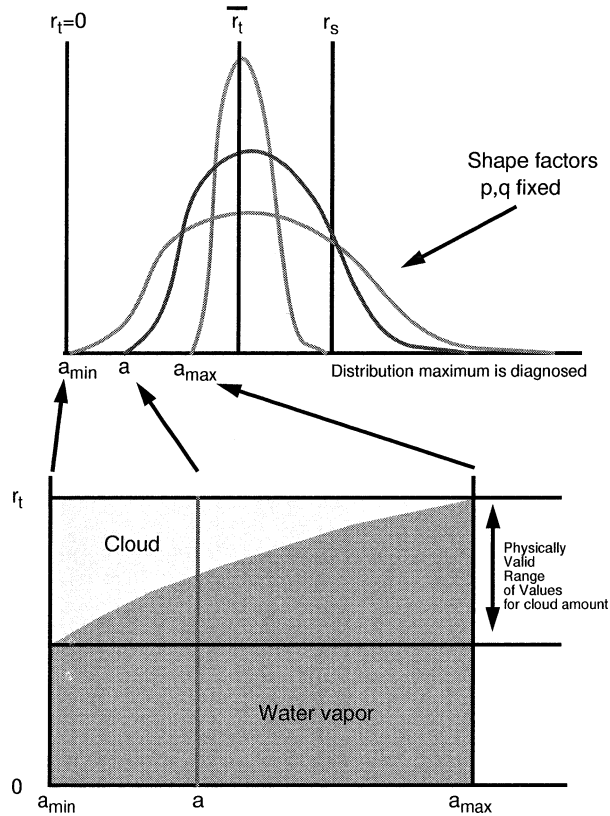
FIG. 4. Schematic of how the scheme functions. (top) Given the shape parameters p and q, the form of the PDF is known. Additionally, the mean of the PDF is equal to $\overline{r}_t$. Only one distribution width (and therefore one value of the distribution minimum a) will divide r_t correctly between cloud condensate and vapor. This is found by iteration. The two curves representing the physical bounds of the iteration are shown by the lightly shaded PDFs. For the case illustrated with $\overline{r}_t < r_s$, these correspond to $a \geq 0$ and $r_c \geq 0$. (bottom) How the diagnosed cloud condensate mass mixing ratio increases monotonically as a decreases from its maximum (where $b = 0$) to zero. See text for discussion.

pendix). Once a is known, b is simple to diagnose from Eq. (12).

As described so far, the scheme requires the introduction of two additional prognostic equations to govern the evolution of p and q. However, this system as it stands is not closed in two specific situations; clear sky conditions ($\overline{r}_c = 0$) or 100% overcast sky ($\overline{r}_v = r_s$). In both these cases only three independent items of information are available (p, q, and $\overline{r}_t$), leaving one degree of freedom to define. One solution to this problem would be to carry a and b as prognostic equations instead of the water variables $\overline{r}_v$ and $\overline{r}_c$, which would be subsequently diagnosed each time step. In this way the beta distribution would always be defined. However, one possible drawback with this method is that numerical errors in, for example, the advection of the distribution parameters, a, b, p, and q, could translate into relatively larger errors in $\overline{r}_c$ and $\overline{r}_v$, since the latter are integral quantities of the former. Moreover, on a practical level,

changing the status of the water variables from prognostic to diagnostic would increase the complexity of implementation in most current GCMs.

One could also argue that, since the cloud cover is well defined in these two specific situations (i.e., 0 or 1), the fact that the distribution of r_t itself is not known is immaterial. However, we maintain that it is still important to model the status and evolution of the r_t distribution in these cases, since, first the information is useful for a nonbiased calculation of microphysical processes in overcast conditions and also of radiative fluxes, and second, the distribution's evolution during periods of clear or overcast skies will determine exactly when the atmosphere will revert to a partially cloudy state. Therefore, the solution we apply is to carry an additional quasi-prognostic equation for the distribution width $b - a$. The terminology quasi-prognostic is adopted since the predicted value is directly used only in clear sky or overcast conditions, otherwise it is always slaved to the value diagnosed by the iteration process described above. This solution therefore avoids the aforementioned numerical problems and is simple to implement, but also involves a degree of redundancy.

With the addition of this equation, the system is now closed at all times. The remaining task is to specify how physical processes such as deep convection or turbulence affect the evolution of p, q, and $b - a$. For notational ease in the following discussion, we use the terms "variance" and "skewness" interchangeably for the quantities $b - a$ and $q - p$, respectively, which are actually carried by the model.

5. Determining the distribution moments

a. Turbulence

Subgrid-scale vertical turbulent motions are assumed to be dynamically isotropic (in contrast to deep convective overturning where limited-area convective drafts are balanced by large-scale subsidence), and therefore have no production effect on the skewness budget. Since the scheme currently neglects the impact of convective downdrafts, the skewness in the turbulent PBL will be limited and have limited vertical gradients. Therefore, we also neglect the vertical transport of skewness by vertical turbulence. However, previous studies have shown that PBL distribution can also exhibit significant skewness (e.g., Bougeault 1982), and therefore future development of the scheme may also incorporate the effect of nonprecipitating convection on the skewness budget, possibly using a mass flux approach as in Lappen and Randall (2001).

Neglecting the horizontal terms, the equation for the change of variance due to subgrid-scale velocity fluctuations is (Deardorff 1974a; Stull 1988):

$$\frac{\partial \overline{r_t'^2}}{\partial t} = -2\overline{w'r_t'}\frac{\partial \overline{r}_t}{\partial z} - \frac{\partial(\overline{w'r_t'^2})}{\partial z} - \epsilon_{r_t'^2}. \qquad (17)$$

The first term on the right represents the production of variance in the presence of a vertical moisture gradient, the second term represents transport of moisture variance by subgrid eddies, and the last term is the dissipation term. Subgrid-scale fluxes include those due to shallow and deep convection in addition to turbulence, but in this section we concern ourselves only with the contribution of turbulence. No separate closure is required for the turbulence moisture flux $\overline{w'r_t'}$ since this is directly available from the vertical turbulence scheme of the GCM.

We follow Stull (1988) to parameterize the variance flux as

$$\overline{w'r_t'^2} = \Lambda\sqrt{e}\frac{\partial\overline{r_t'^2}}{\partial z}, \tag{18}$$

where e is the turbulent kinetic energy, also available from the model's vertical turbulence scheme, and Λ is a mixing length-scale, which is defined as $\Lambda = lS_r$, where S_r is a stability function and l is defined according to Blackadar (1962) as

$$l = \frac{kz}{1 + kz/\lambda}. \tag{19}$$

Here k is von Kármán's constant, and λ is the asymptotic mixing length, set to 150 m in the PBL. Roeckner et al. (1996) provides details of stability function formulation S_r.

Since the model carries the distribution width, $b - a$, rather than the variance in its closure, the production term must be converted using Eq. (9). The turbulent production does not affect the distribution shape parameters, thus it can be simply written:

$$\frac{\partial(b - a)}{\partial t} = -\frac{\eta}{(b - a)}\overline{w'r_t'}\frac{\partial\overline{r_t}}{\partial z} - \Lambda\sqrt{e}\frac{\partial(b - a)}{\partial z}$$
$$- \epsilon_{b-a}, \tag{20}$$

where $\eta = (p + q)^2(p + q + 1)(pq)^{-1}$.

We now consider the dissipation term, which we will derive directly in terms of the distribution width ($b - a$) and is defined as a Newtonian relaxation as is usual (e.g., Deardorff 1974a; Stull 1988; Garratt 1992):

$$\epsilon_{b-a} = (b - a)\left(\frac{1}{\tau_v} + \frac{1}{\tau_h}\right). \tag{21}$$

The timescale has been split into components. The first, τ_v, represents the dissipation due to 3D turbulence, in the PBL and in the neighborhood of deep convection cores for example, while the second component represents the dissipation by larger-scale 2D horizontal eddies caused by horizontal wind shear instability, which will be present even if strong stable temperature stratification suppresses vertical motions.

The timescale of the 3D turbulent dissipation τ_v is defined in terms of the turbulent velocity scale $\sqrt{e}$ and the turbulent length scale (Garratt 1992)

$$\tau_v = \frac{\kappa l}{\sqrt{e}}, \tag{22}$$

where κ is a constant, for which Garratt (1992, p. 253, Table 8.2) suggests a value of 7.44. This timescale is typically fast, and in the PBL the primary balance is between turbulent production and dissipation (e.g., Deardorff 1974b).

Above the PBL, the turbulent eddy scale is no longer relevant for describing the horizontal scale of r_t', and therefore (22) is applied only below the diagnosed PBL top. For shallow cumulus it is possible that cloud depth could be used, following Lenderink and Siebesma (2000), but this would also not be appropriate for deep convective regimes where the horizontal scales of the subsidence regions surrounding convective cores are much larger than the depth of the cores themselves. Therefore above the PBL, it is assumed that the variance in total water occurs over length scales comparable to the horizontal grid size of the GCM, Δ_x. It is possible that by taking the convection type (i.e., shallow or deep) and mesoscale organization in account, improvements could be made on this assumption. Since the grid-mean turbulent velocity scales are usually very limited above the PBL, the mixing due to large-scale horizontal eddies will be dominant. To parameterize these we use the standard Smagorinsky approach (Smagorinsky 1963) and define

$$\frac{\partial(b - a)}{\partial t} = -\frac{1}{\rho}\frac{\partial}{\partial x}\left[\rho\nu\frac{(b - a)}{\Delta_x}\right], \tag{23}$$

where it has been assumed that the subgrid-scale horizontal r_t gradient can be approximated by $(b - a)\Delta_x^{-1}$, and where ν is the viscosity, defined in terms of the horizontal wind shear in the normal way:

$$\nu = (C_s\Delta_x)^2\sqrt{\left(\frac{\partial u}{\partial x}\right)^2 + \left(\frac{\partial v}{\partial y}\right)^2}, \tag{24}$$

where C_s is a constant that we set to 0.23 (for discussion, see Mason and Callen 1986; Mason and Brown 1999). It should be emphasized that this horizontal eddy flux of moisture is completely subgrid-scale and should not be confused with the horizontal mixing of prognostic quantities between adjacent model grid points already represented in the horizontal diffusion schemes of large-scale models.

Assuming that horizontal subgrid-scale variations in density can be neglected, this gives a horizontal mixing timescale of

$$\tau_h^{-1} = C_s^2\sqrt{\left(\frac{\partial u}{\partial x}\right)^2 + \left(\frac{\partial v}{\partial y}\right)^2}. \tag{25}$$

For a wind shear of 2×10^{-5} s^{-1}, this gives a mixing timescale of roughly 10 days, broadly in accordance with Pierrehumbert and Yang (1993) and Emanuel and Pierrehumbert (1996) for high wavenumbers.

Since this mixing will also reduce the skewness of the distribution, tending with time toward a symmetric one, the same timescale relaxation is applied to q:

$$\frac{\partial q}{\partial t} = (q_0 - q)\left(\frac{1}{\tau_v} + \frac{1}{\tau_h}\right), \quad (26)$$

where q_0 defines the shape of the final distribution.

The influence of the turbulence on the cloud and vapor quantities must also be explicitly taken into account. A calculation of $\Delta\bar{r}_c$ and $\Delta\bar{r}_v$ due to turbulence is obtained by stepping the quantities $b - a$ and q forward by one time step Δt (using an implicit solution as described in the appendix), using Eqs. (20) and (26) only, in conjunction with $\Delta\bar{r}_t = 0$. The rate of change of the water quantities is thus:

$$\frac{\partial\bar{r}_v}{\partial t} = \frac{\Delta\bar{r}_v}{\Delta t} \quad (27)$$

$$\frac{\partial r_l}{\partial t} = \frac{r_l\Delta\bar{r}_c}{(r_l + r_i)\Delta t} \quad (28)$$

$$\frac{\partial r_i}{\partial t} = \frac{r_i\Delta\bar{r}_c}{(r_l + r_i)\Delta t}. \quad (29)$$

b. Convection

Convective towers directly detrain cloud condensate to form upper-level cirrus anvil cloud and extensive stratiform cloud coverage. Cumulus parameterization schemes already represent the transport of the mean quantities of water vapor and cloud, but it is clear that the deep convective process also increases the variance of the water vapor by introducing localized perturbations (Liao and Rind 1997). Moreover, it was seen in the analysis of the CRM data that since clouds detrain high mixing ratios of cloud condensate, they also introduce a significant positive skewness into the distribution of cloud. In the same way, the presence of convective scale downdrafts that inject dry air into the boundary layer resulted in a negative skewness of the distribution. However, since the influence of downdrafts is largely restricted to the PBL, the decision was made to initially neglect their influence. Only positively skewed or symmetrical distributions are therefore represented and this therefore allows the shape parameter p to be held constant, reducing the number of additional prognostic equations by one. It is straightforward to relax this restriction and introduce a further prognostic equation for p in the future.

The simplest approach is to relate the increase in skewness to the detrainment of cloud condensate, readily available from most current cumulus parameterizations, giving

$$\frac{\partial q}{\partial t} = \frac{K}{\bar{\rho}r_s}\frac{\partial}{\partial z}(M^{cu}r_c^{cu}), \quad (30)$$

where K is a dimensionless constant, M^{cu} is the updraft mass flux, and r_c^{cu} is the mean cloud water in the convective updrafts. Here the implicit assumption is made that $r_c^{cu} \gg \bar{r}_c$.

In cases of overcast sky, the effect of deep convective detrainment on the distribution width, $b - a$, should also be taken into account. Since the increase in variance is associated with increased skewness, the change in the distribution minimum is much smaller than the change is the maximum, that is, $|\Delta a| \ll |\Delta b|$. Figure 5 illustrates this for the CRM data, which shows that the variability in a exceeds only that of b in the PBL due to the action of downdrafts, which are currently neglected in this scheme. The simplification is therefore made that $|\Delta a| = 0$, which using (12) in conjunction with the new value of q due to convective processes, $q + \Delta q_{conv}$, calculated from (30), gives:

$$\frac{\partial(b - a)}{\partial t}$$
$$= \frac{(\bar{r}_t - a)(p + q + \Delta q_{conv})p^{-1} - (b - a)}{\Delta t}, \quad (31)$$

where Δt is the model time step. This simple treatment of the effect of the convection could be replaced by a more comprehensive mass flux approach following Lenderink and Siebesma (2000) or Lappen and Randall (2001).

c. Large-scale condensation

In addition to convective and turbulent processes, cloud can also be created/destroyed by cooling/warming and by net convergence/divergence of total water. This has to be consistent with the PDF adopted for r_t. In order to simplify this, the change in total water due to large-scale advection and other processes Δr_t is added uniformly to the total water distribution. This implies that the cloud mixing ratio after one time step, $(\bar{r}_c)_{t+\Delta t}$, can be calculated by a simple translation of the PDF, as the shape factors p and q are not changed. If Δr_s represents the change in the saturation vapor mixing ratio due to the temperature change, then $(\bar{r}_c)_{t+\Delta t}$ is derived directly from (14) as

$$(\bar{r}_c)_{t+\Delta t} = (\bar{r}_t - a)[1 - I_f(p + 1, q)]$$
$$+ (a + \Delta\bar{r}_t - r_s - \Delta r_s)[1 - I_f(p, q)], \quad (32)$$

where $f = (r_s + \Delta r_s - a - \Delta\bar{r}_t)(b - a)^{-1}$.

d. Microphysics

Further processes that should be considered are the microphysical pathways between the various water categories that are represented in the GCM cloud scheme. If a cloud is heavily precipitating, for example, the loss of the cloud water will reduce both the distribution skewness and variance. The task of representing this is
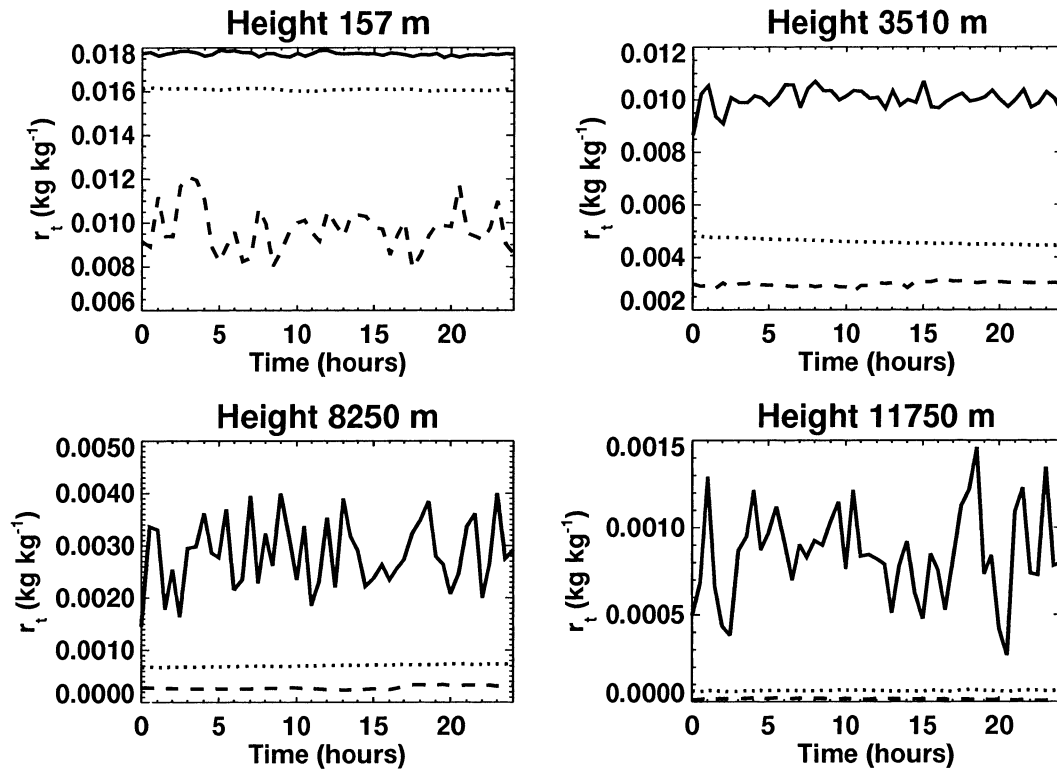
FIG. 5. Time series of minimum a (dashed line), mean (dotted), and maximum b (solid) of r_t distribution at various heights for the CRM data.

simplified for the distribution variance because in partially cloudy conditions the variance is a diagnostic quantity. The microphysical processes will therefore indirectly alter the distribution width through their action on $\bar{r}_c$ and $\bar{r}_v$.

In contrast to the variance equation, the skewness of the distribution must be explicitly considered. To accurately determine the skewness change, Eq. (13) and (14) would need to be solved for the forward-stepped values $\bar{r}_c + \Delta \bar{r}_c^{\text{micro}}$ and $\bar{r}_v + \Delta \bar{r}_v^{\text{micro}}$, where $\Delta \bar{r}_c^{\text{micro}}$ and $\Delta \bar{r}_v^{\text{micro}}$ represent the change over one timestep due to microphysical processes. However, this would require iteration to solve, involving the nonlinear shape function q, therefore increasing the numerical expense of the scheme. It is however possible to make an approximation by considering the distribution maximum b. If microphysical processes remove all cloud within one time step, then the change in the distribution maximum is simply $\Delta b = \bar{r}_s - b$. A linearized relationship is therefore assumed with

$$\Delta b^{\text{micro}} = \frac{\Delta \bar{r}_c^{\text{micro}}}{\bar{r}_c}(b - \bar{r}_s). \quad (33)$$

As for the convection source of variance, Eq. (31), the assumption is again made that for microphysical processes $|\Delta a| \ll |\Delta b|$, which in conjunction with (33) allows the change in skewness to be expressed via (12) as

$$\Delta q^{\text{micro}} = \frac{\left[b + \dfrac{\Delta \bar{r}_c^{\text{micro}}}{\bar{r}_c}(b - \bar{r}_s)\right]p}{\bar{r}_t - a} - (p + q). \quad (34)$$

e. Tunable constants

The scheme as it stands thus has two tunable constants: K, which specifies how quickly detraining convection increases the skewness of the distribution, and q_0, which defines the shape of the symmetric distribution eventually adopted in the absence of convection.

As discussed earlier, the distribution will tend to a symmetrical one, due to horizontal mixing, and therefore our choice for q_0 will also be imposed on the shape parameter p, which is held constant in the first version of the scheme. We select $q_0 = p = 2$, which is close to the lower limit of 1, which defines the bell-shaped beta distribution regime in order to give a distribution that meets the zero line sharply without extensive tails. An example of the $p = q = 2$ beta distribution was given in Fig. 2. Based on model tuning, K is set to 10.

f. Summary

To summarize, a prognostic equation is added to the GCM to represent the evolution of the beta distribution

shape factor q, which can be related to the skewness of the total water distribution:

$$\frac{Dq}{Dt} = \frac{K}{\bar{\rho}r_s}\frac{\partial}{\partial z}(M^{cu}r_c^{cu}) + \frac{\Delta q^{micro}}{\Delta t}$$

$$+ (q_0 - q)\left(\frac{1}{\tau_v} + \frac{1}{\tau_h}\right). \tag{35}$$

The other shape factor p is constant in this implementation. Water vapor, ice and liquid cloud mass mixing ratio are predicted as previously. Knowing p and q, in addition to the water vapor and cloud condensate mass, defines the beta distribution PDF, allowing cloud cover to be diagnosed using $C = 1 - I_{(r_s-a)/(b-a)}(p, q)$.

For clear sky or overcast conditions ($C = 0$ or 1) it is necessary to have one additional quantity to define the PDF. Therefore an additional equation for the distribution width (related to the variance of total water) is added:

$$\frac{D(b-a)}{Dt}$$

$$= \frac{(\bar{r}_t - a)(p + q + \Delta q_{conv})p^{-1} - (b-a)}{\Delta t}$$

$$- \frac{\eta}{(b-a)}\overline{w'r_t'}\frac{\partial \bar{r}_t}{\partial z} - \Lambda\sqrt{e}\frac{\partial(b-a)}{\partial z}$$

$$- (b-a)\left(\frac{1}{\tau_v} + \frac{1}{\tau_h}\right). \tag{36}$$

In partially cloudy conditions the distribution width is diagnosed and the prognostic quantity is slaved to this diagnosed value. Both parameters are advected by the large-scale flow. Equations (27), (28), (29), and (32) are also added to the water prognostic equations, with the relevant heat added to the thermodynamical budget.

The function of the scheme is summarized schematically in (6) and (7) which depict, in an idealized way, the state of the model grid cell, along with the associated PDF of r_t. Figure 6 shows the situation of convection detraining at a model layer. At first the grid cell contains no cloud (a), and the PDF is narrow, almost symmetrical and lies completely in the region to the left of r_s. Convection then detrains cloud mass at this model gridcell (b), locally moistening, while at the same time the compensating subsidence reduces the relative humidity generally (Randall and Huffman 1980). In addition, the new scheme also increases the positive skewness of the PDF in response. Thus the scheme can predict that a relatively small part of the domain is covered by cloud, some of which has large condensate mass values due to the long distribution tail. If the convection then ceases, horizontal mixing (and precipitation processes) will reduce the mean cloud condensate, and the skewness will also reduce (c). Evaporation of cloud will increase the relative humidity. Thus the distribution becomes
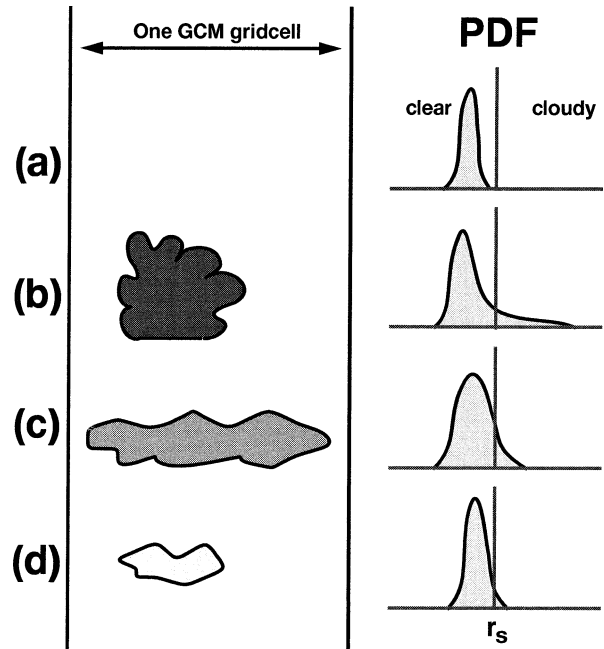
FIG. 6. Schematic of how cloud development is represented in new scheme. (left) An idealized state of the model grid cell; shading indicates cloud thickness. (right) The associated PDF of r_t represented in the scheme, with the saturated value r_s marked as the vertical line.

more symmetrical, and the cloud fraction can increase. This, in effect, is representing the transition from a limited area, optically thick, anvil cloud shortly after deep convective development, to a situation of thinner cirrus covering a larger proportion of the grid cell. Finally, since $\bar{r}_t < r_s$, even if precipitation loss ceases, horizontal mixing will reduce the distribution width further and the cloud dissipates (d).

In the above example, the relative timescales of the cirrus growth and dissipation will, of course, depend on the relative incipient values of vapor and cloud. For instance, if the mean total water r_t exceeds the saturation mixing ratio initially, the cloud will not dissipate and the grid point will tend to overcast conditions (ignoring losses due to precipitation formation for the sake of argument). This is portrayed in Fig. 7, where the inital conditions are overcast, and the entire PDF lies in the cloudy region (a); hence the relative humidity (RH) is exactly 100%. If convection occurs in this grid cell it is possible that the drying associated with the subsidence will cause the RH to fall below 100% in some parts of the grid cell. Meanwhile the cloud condensate and skewness will increase as previously. Hence the PDF will have the appearance depicted in (b), where part of the domain becomes clear from cloud, while the other part will contain very thick cloud. As the convective cloud mixes with the surrounding air (PDF narrowing and becoming more symmetrical), it is likely that overcast conditions will return (c).
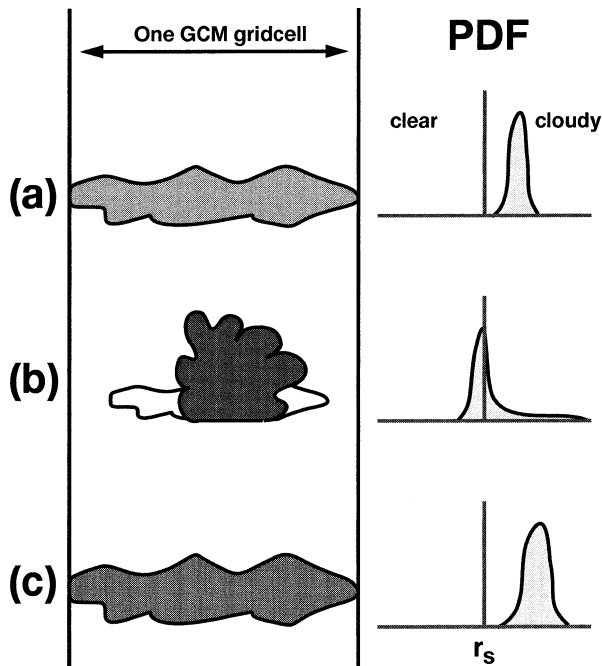
FIG. 7. As for Fig. 6 but for the case where $\bar{r}_t > r_s$.

6. Implementation in a large-scale model

The parameterization has been implemented into the latest version of the ECHAM GCM (Roeckner et al. 1992, 1996) called ECHAM5, briefly described in the appendix. The aim of this section is to illustrate the function of the parameterization in the GCM. More extensive validation will be performed in a future publication.

a. One-month experiment

A short 4-week integration of the 3D GCM using T42 resolution and 19 vertical levels was conducted to allow the examination of high temporal resolution statistics at individual grid points and detailed snapshots of global fields.

To illustrate the general function of the scheme, Fig. 8 shows a snapshot of the cloud cover, along with the skewness of the total water at model level 6 (approximately 160 hPa) taken on the final day of the integration. The panels clearly show how skewness values are highest in regions of deep convection detrainment, often exceeding unity. Away from the Tropics, the skewness is almost zero at this height, with a symmetrical distribution. As expected, the variance (not shown) increases toward the Tropics as the temperature and humidity increases, but the field also reveals high variance values associated with convective activity. The signature of deep convection is apparent in the skewness and variance fields long after the associated cloud has dissipated.

The second snapshot focuses on the Pacific Ocean (Fig. 9), and reveals that at 950 hPa the skewness is

instead highest away from the Tropics, in the midlatitude and subtropical regions that are subject to shallow convection. The distribution width is very closely correlated to the variance, and marked by localized peaks in tropical areas in which turbulence activity is higher.

Time series are analyzed from two grid points for different cloud regimes to better illustrate the scheme's behavior. The grid points are taken from the western Pacific to illustrate the behavior in a deep convective regime, and just off the west coast of South America for a stratocumulus regime. The exact location of the grid points is shown in Fig. 10.

1) WESTERN PACIFIC

A time–height plot of cloud cover is shown for the simulation in Fig. 11, which reveals a prevalence of high cloud throughout the period produced by deep convection detraining at heights between 300 and 100 hPa. Boundary layer cloud is occasionally produced by shallow convection. To gain a clearer view on how the scheme is actually functioning, Fig. 12 shows the evolution of cloud cover, the maximum and minimum value for r_t, r_s, ice cloud r_i, relative humidity (RH), and the skewness and standard deviation of r_t derived from the beta distribution parameters. The data is taken at level 7 of the model, corresponding to a pressure of 190 hPa, in the middle of the height range of deep convective detrainment. The large increase in variance when cloud is formed is apparent, which remains for a considerable time while $\bar{r}_t > r_s$, since mixing acts to increase cloud cover in these cases. The skewness is considerable at this level, reaching levels of 0.8, although this is lower than the values reported by Xu and Randall (1996a), and remains so throughout this period. The RH undergoes substantial variations, ranging from 20% to saturation. This contrast between convectively active and break periods has also been documented in observations (e.g., Brown and Zhang 1997).

The average profiles for the days 10–25 of the experiment are given in Fig. 13. The cloud cover produced by the scheme of Xu and Randall (1996a) is also shown for comparison, which we refer to here as the XR scheme for brevity. It is seen that the mean cloud fraction is almost identical throughout the troposphere, except in the upper part of the detrainment zone between approximately 300 and 100 hPa, where the present scheme gives a cloud fraction 10% higher than that of XR. The reason for this is probably the lower skewness that the present scheme attains, compared to the CRM data upon which the XR scheme was based. With a smaller skewness more cloud points are required to obtain the grid-mean cloud mass $\bar{r}_c$. This could be a result of the fact that the skewness of the beta distribution has an upper bound, which is perhaps insufficient for the deep convective detrainment zone. It should be strongly emphasized, however, that this comparison where the XR scheme is used passively, tests only the suitability

Cloud Cover: Day 28 at 160 hPa

Skewness of Total Water
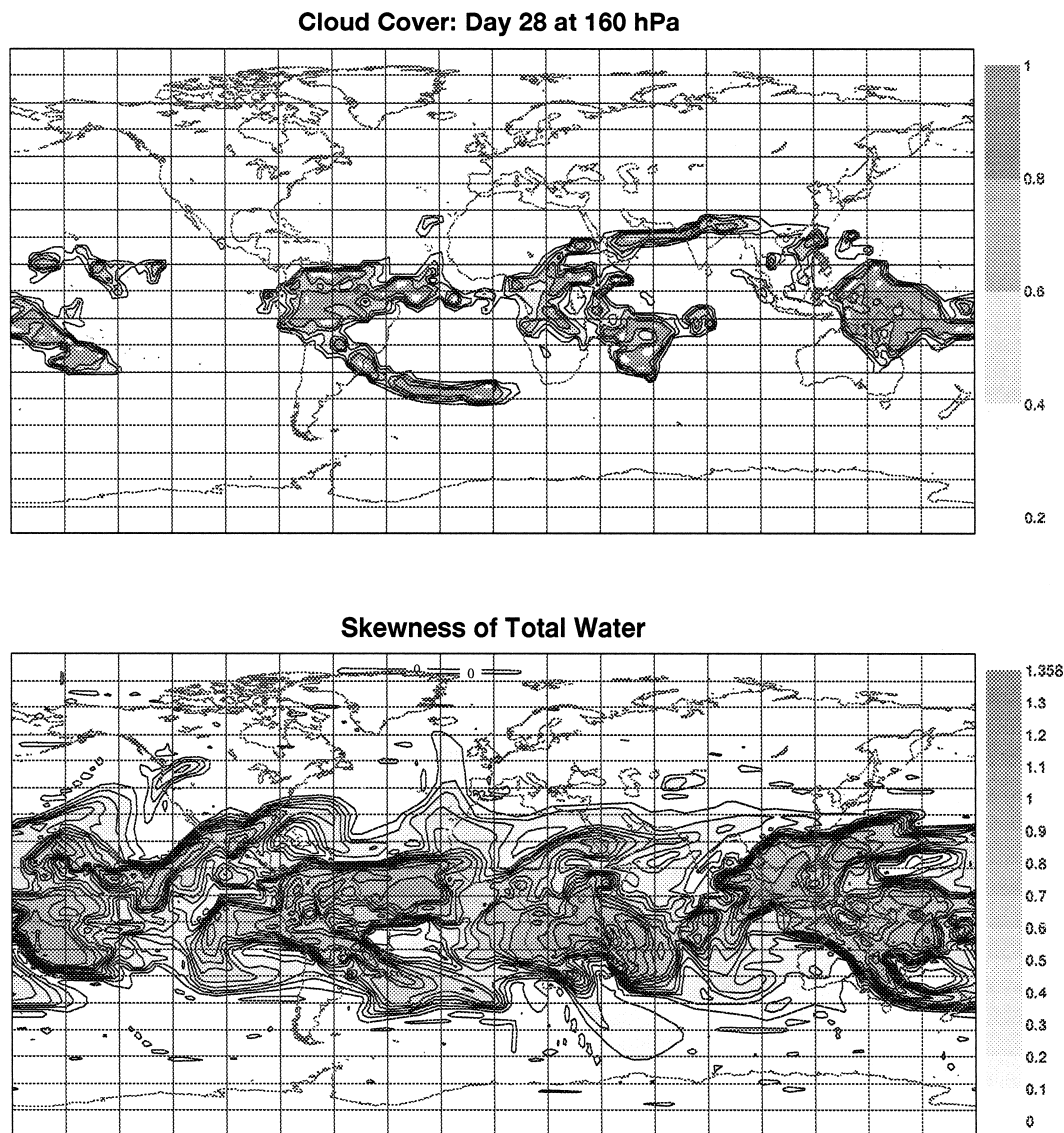
FIG. 8. (top) Global cloud cover and (bottom) skewness at model level 6 (160 hPa) at day 28 of the 4-week experiment.

of the PDF. It illustrates that the beta distribution would provide a good fit to the majority of the data of Xu and Randall (1996a). Although the cloud fraction predicted by the two schemes is very similar, it does not imply that using the diagnostic XR formulation would achieve the same simulation in the GCM. This is because the latter scheme does not include the influence of processes such as turbulence or convection on the distribution moments, such as in the present scheme and thus its use actively would produce a completely different evolution of the model fields.

The other panels of the plot reveal that the scheme functions as one would expect, with decreasing variance with height marked by peaks at the convective detrainment zones, RH maxima at the top of the well-mixed layer and the deep convective detrainment zone, the latter of which also coincides with the skewness maximum, and a reasonable distribution of the ice and liquid water mean mixing ratios, with a second liquid water peak corresponding to the level at which limited low-level cloud occurs.

2) STRATOCUMULUS REGIME

In the second example from the GCM we briefly examine a grid point to the west of the South American coast, in a region that typically experiences stratocumulus cloud. A low-level cloud layer is indeed formed at this location (not shown) although it is poorly resolved with the climate model's standard vertical resolution.

Examining the evolution of cloud cover and the r_t

Total Water Distribution Width (g/kg) Day 28 at 950 hPa
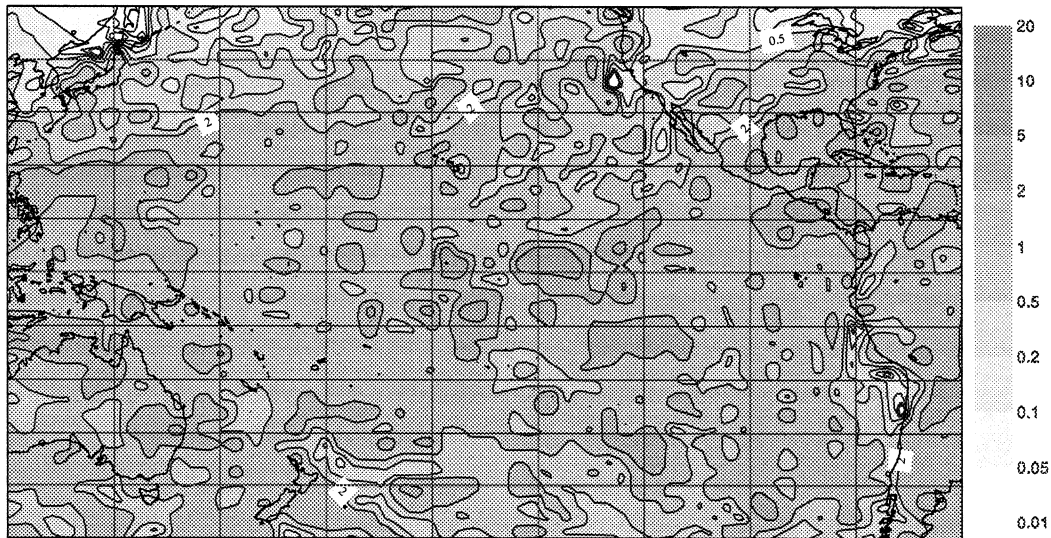
Skewness of Total Water
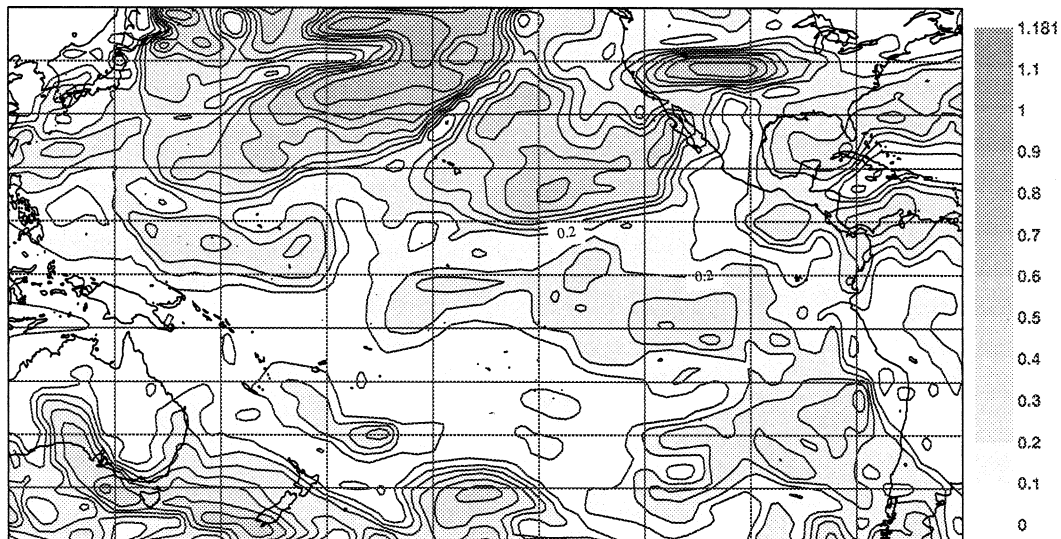
FIG. 9. (top) Distribution width ($b - a$) and (bottom) skewness at model level 16 (950 hPa) at day 28 of the 4-week experiment for the Pacific basin.

distribution minimum and maximum compared to r_s for an 8-day section through the cloud at model level 17 (970 hPa) reveals the way turbulence can act to create or destroy cloud in the new scheme (Fig. 14). At day 12, the distribution minimum exceeds the saturation mixing ratio and the cloud cover is correspondingly 100%. About 18 h later, turbulent activity acts to increase the distribution width considerably, breaking up the overcast cloud layer, with the cloud cover falling briefly below 40%. The turbulent dissipation of variance quickly acts to reduce the distribution width, and since $\bar{r}_t > r_s$ at this time, this increases the cloud fraction

back toward overcast conditions in the following few hours. This occurs repeatedly over the following few days. At day 17 the model at this grid point dries considerably, and clear sky conditions prevail. Now the situation is reversed, and the occurrence of increased turbulent activity with an associated distribution width increase on day 17.7 causes the distribution maximum to exceed r_s, creating cloud with short lifetimes. Thus the creation of small-scale cloud at the top of boundary layer turbulent eddies is also seen to be well represented in the new scheme, despite the coarse vertical resolution used.
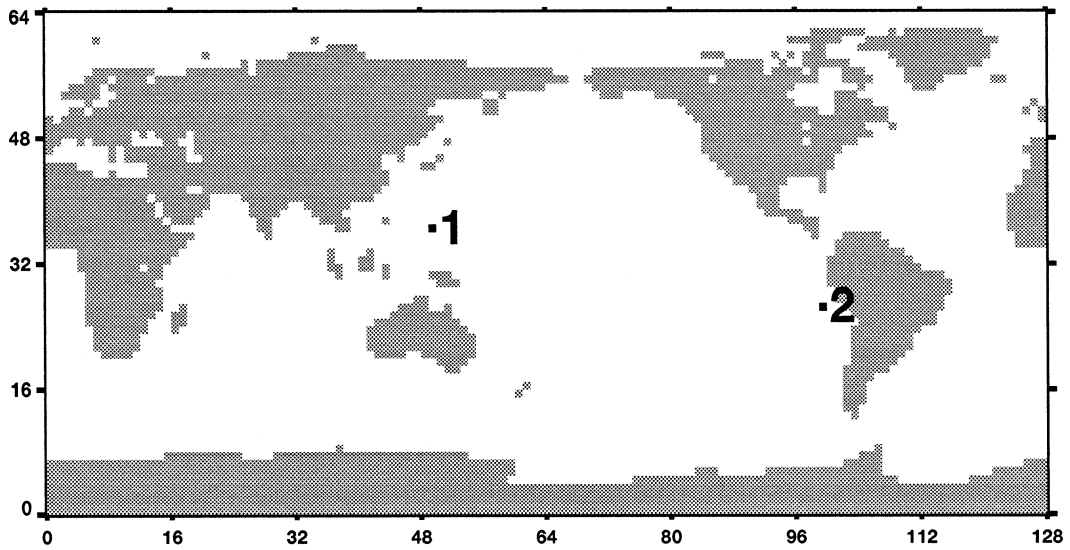
FIG. 10. Global map showing land–sea mask for climate model and the location of the two grid points analyzed in the western Pacific warm pool (1) and off the west coast of South America (2).

Cloud Cover

contours: 0.20 0.40 0.60 0.80 1.00
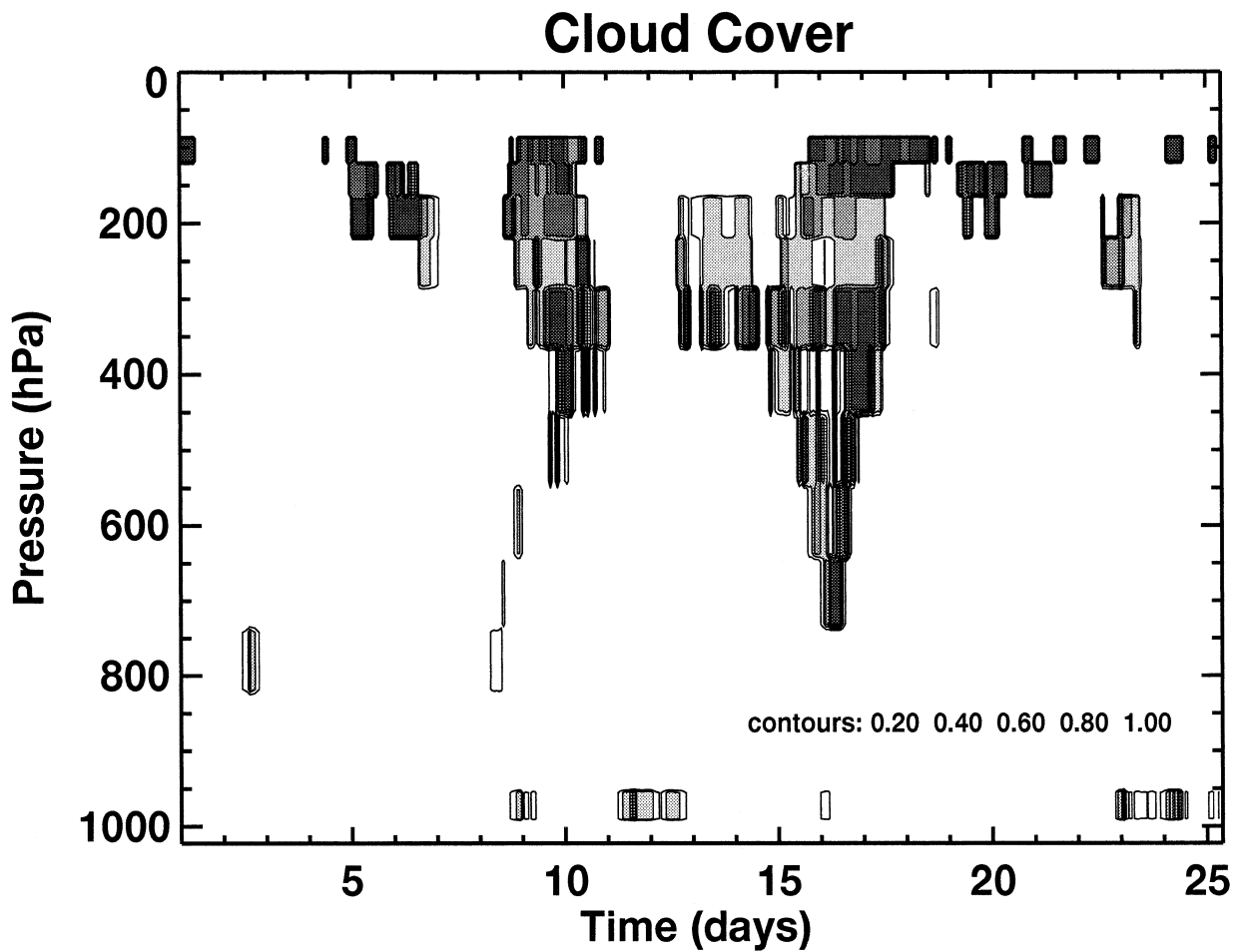
FIG. 11. A 25-day time–height section of cloud fractional cover at the western Pacific grid point. Cloud-fraction contour values are 0.2, 0.4, 0.6, 0.8, and 1.0.
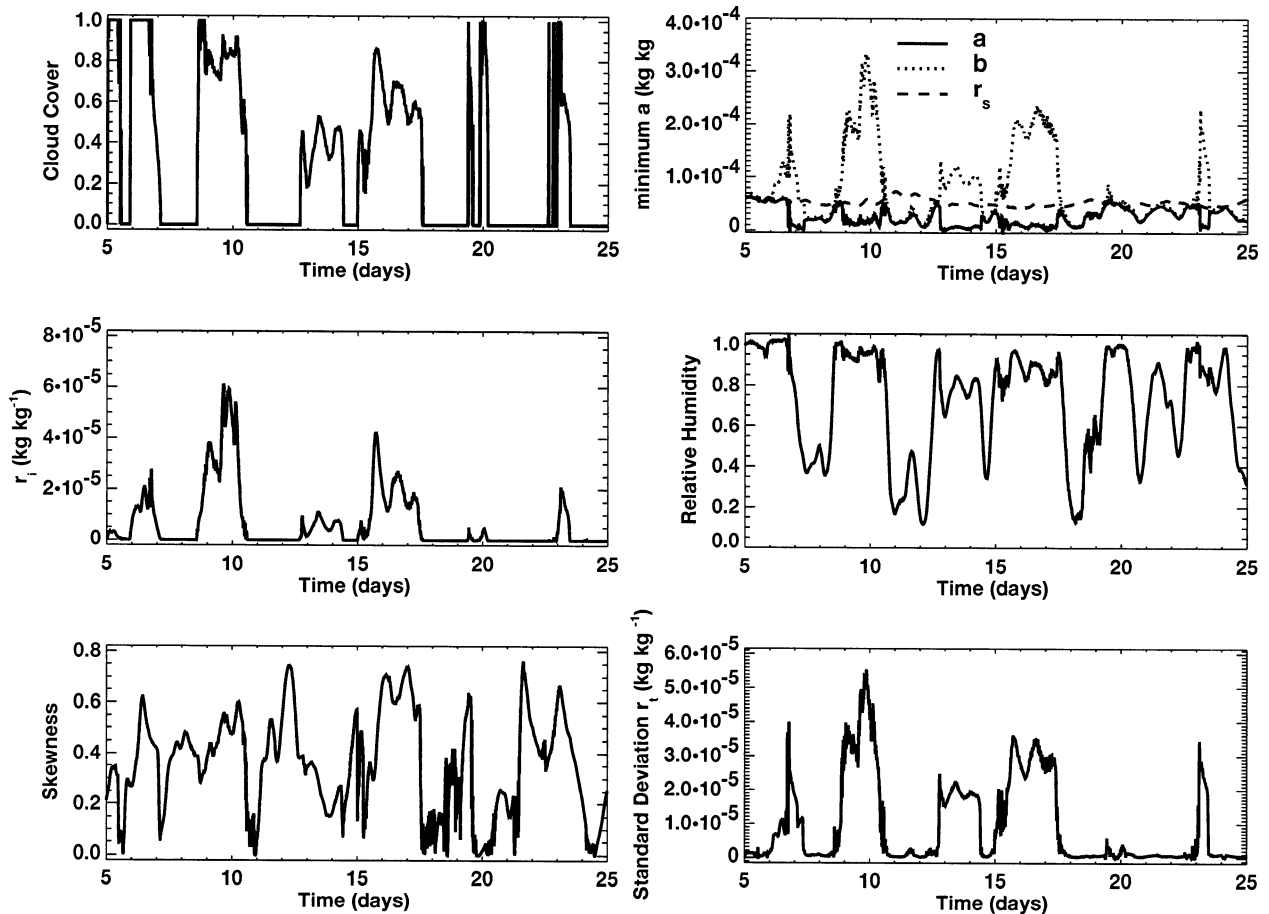
FIG. 12. (upper left) Time series of cloud cover, (upper right) the minimum and maximum values of total water (r_t) (*a* and *b*, respectively) and the saturation mixing ratio (r_s), (middle left) ice cloud r_i, (middle right) relative humidity (RH), (lower left) skewness, and (lower right) standard deviation of r_t. The data are from level 7 of the model at the western Pacific grid point, corresponding to a pressure of 190 hPa.

In the earlier review of observational literature, it was stated that Wielicki and Parker (1994) found liquid water paths to be exponentially distributed without a distribution peak in low cloud cover conditions while in high cloud cover cases the distribution was more Gaussian-like, usually with a distinct peak. The new parameterization reproduces this behavior (not shown) for obvious reasons. When cloud cover is high the total water distribution lies mostly to the right of the saturation point, and a peak in liquid water path is produced. For small cloud fractions only the distribution tail is observed in terms of liquid water path observations.

b. Climate experiments

Two 20-yr climate simulations were performed at T42 resolution initialized on 1 January 1979. One experiment uses the new prognostic cloud scheme described in this paper, and the second instead parameterizes cloud cover with the previous diagnostic relative humidity scheme of Lohmann and Roeckner (1996).

The mean total cloud cover from these experiments is compared to the International Satellite Cloud Climatology Project (ISCCP) total cloud cover data between 1983 and 1990 (Rossow and Schiffer 1991; Fig. 15). It is apparent that both schemes capture the climatological distribution of cloud cover reasonably well, but also that both suffer from similar biases. There is an overestimation of cloud in the tropical and subtropical Pacific, and also over equatorial land regions, especially Africa and the Americas. These errors are closely linked with the activity of deep convection, with convection apparently persistently overactive in a narrow belt over the intertropical convergence zone, for example.

Generally, the model has a tendency to have positive biases in regions of high cloud cover, and negative biases in regions of low cloud cover. One possible reason the contrast could be too large is an overrepresentation of cloud–radiative feedback, which has been postulated as important in intensifying tropical dynamical circulations such as the Hadley and Walker Cells (Raymond 2000) and was found to strongly organize convection on small scales in CRM experiments (Tompkins and
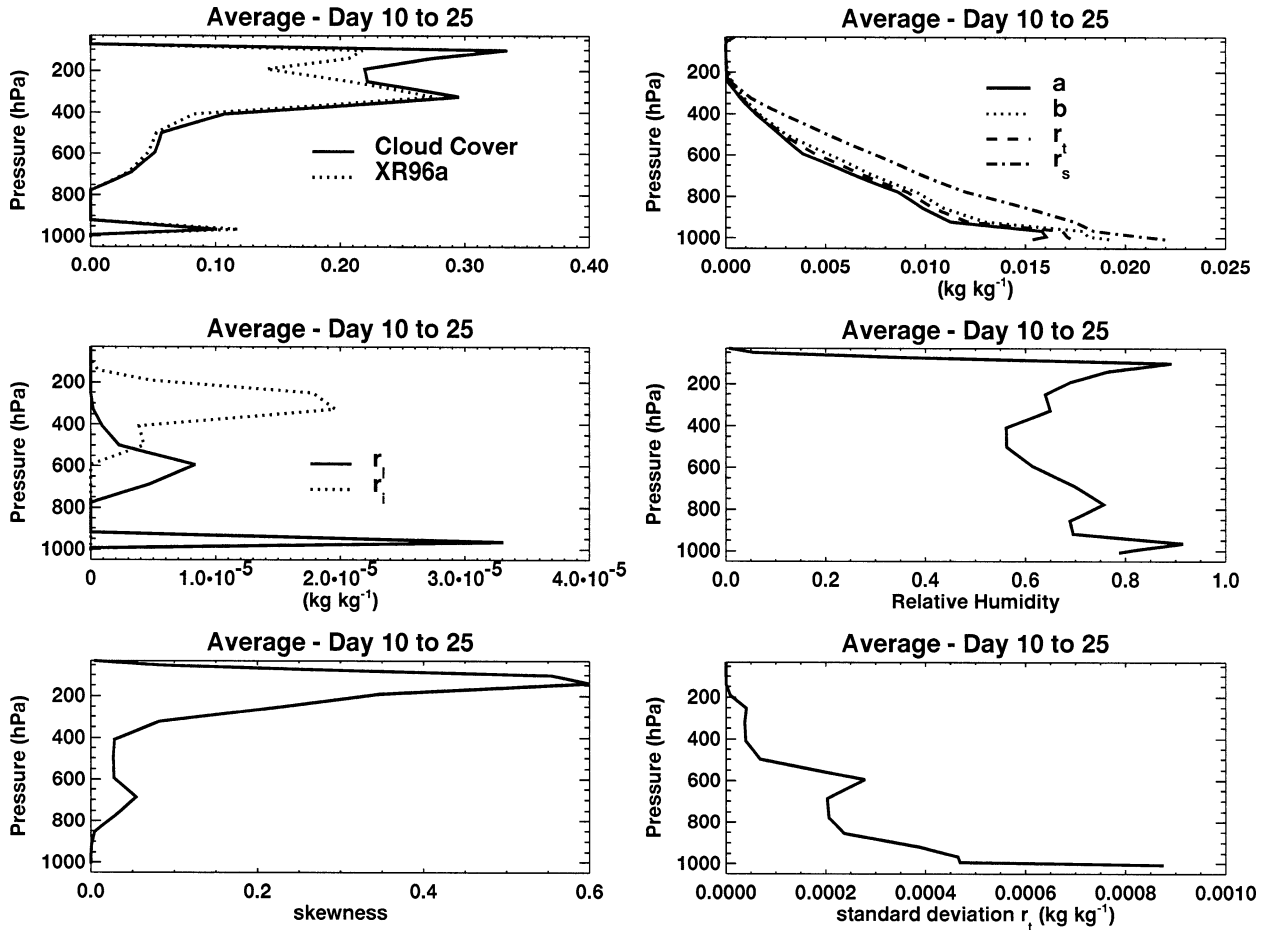
FIG. 13. As for Fig. 12 but showing the mean for days 10–25. The cloud cover calculated using the scheme of Xu and Randall (1996a) is superimposed, and the mean liquid mass mixing ratio is also shown in addition to cloud ice.

Craig 1998). Bergman and Hendon (2000) estimate that cloud–radiative feedback contributes 20% to low-level dynamical circulations. An additional glaring bias in the simulations is the lack of cloud in the stratocumulus regions in the eastern Pacific and Atlantic Oceans.

Comparing the two schemes (lower-right panel), it is found that the prognostic scheme results in an almost global improvement in the cloud simulation, with the possible exception of the polar regions, for which the observational data is less reliable. The cloud contrast is systematically reduced, with reduced biases over the subtropical oceans, and to a limited extent over tropical Africa. The most noticeable improvement to the cloud simulation lies in the stratocumulus regions off the west coasts of all major continents, which show cloud cover increases of up to 25%, although these cloud regimes are still underrepresented. The direct link with the physical components of the model, such as the turbulence scheme, permits such localized improvements to the simulation, as conjectured in the introduction.

A good match is also reproduced when the model liquid water path (LWP) and long-wave cloud forcing

are compared to the Special Sensor Microwave/Imager (SSM/I data; mean for 1987–91; Greenwald et al. 1993; Fig. 16) and the Earth Radiation Budget Experiment (ERBE) data (1985–88) (Ramanathan et al. 1989; Fig. 17), respectively. In both cases the difference between the new prognostic scheme described here and the previous diagnostic scheme is marginal, although a noticeable improvement is seen for the LWP. It should be stressed that these comparisons are not regarded as a rigorous validation of the cloud scheme, although they do give confidence that the GCM including the new scheme reproduces certain cloud statistics reasonably well for the present climate.

7. Conclusions

A new prognostic scheme has been developed for large scale models that represents the subgrid-scale variability of water vapor and cloud, and is used to diagnose cloud cover in the spirit of previous statistical schemes. The advantage of statistical schemes is that, as long as a reasonable PDF form is used, the predicted cloud cov-
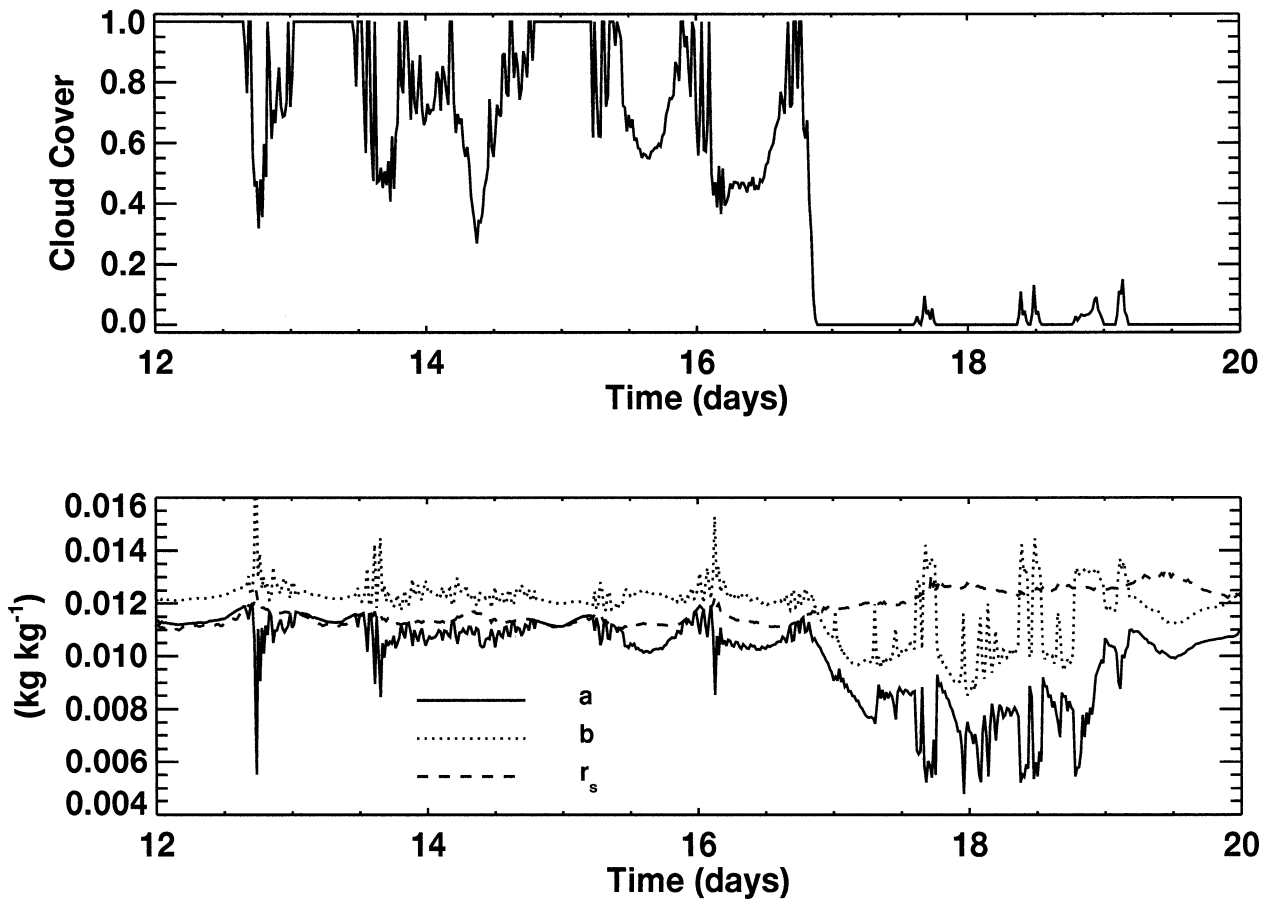
FIG. 14. (top) Time series of cloud cover. (bottom) The minimum and maximum value for r_t, (a and b, respectively) and the saturation mixing ratio (r_s). The data are from level 17 of the model at the eastern Pacific grid point, corresponding to a pressure of approximately 970 hPa.

er is always consistent with the relative amounts of water vapor and cloud condensate in the model.

The scheme has several original aspects. First, a PDF has been used to describe the variability of total water that has the properties of being bounded and can flexibly produce both positively and negatively skewed distributions in addition to Gaussian-like symmetric distributions. The PDF was able to reproduce the r_t distribution from high-resolution CRM tropical deep convection experiments reasonably well, with the exception that the small areas of large cloud condensate were sometimes underestimated. A brief review of the observational literature appeared to show that the beta function could be reasonably applied in the majority of observed cases, in a variety of atmospheric conditions.

Another new aspect of this scheme is that it introduces the higher-order moments of skewness and variance as separate prognostic variables, so that the distribution of the total water r_t evolves in time. Specifically, the physical processes affect the distribution of r_t as follows:

• Detrainment from deep convective updrafts increases the positive skewness of the total water distribution and also the distribution width.
• Vertical turbulence increases the width of the distribution in the presence of a vertical r_t gradient, transports variance, and dissipates variance and skewness in the PBL on an turbulent eddy-related timescale.
• Microphysical processes reduce the skewness of the distribution and implicitly the distribution width.
• Horizontal subgrid-scale turbulence caused by horizontal wind shear instability decreases the distribution skewness and variance, albeit on a much slower timescale than the PBL dissipation by vertical turbulence.

The new scheme has been successfully implemented into the Max Planck Institute global climate model, ECHAM5, and produces realistic distributions of clouds. The scheme improved various aspects of the climate simulation, most noticeably producing a marked improvement in the representation of stratocumulus regimes.

One further advantage of a prognostic statistically based scheme is that it can be easily expanded to include
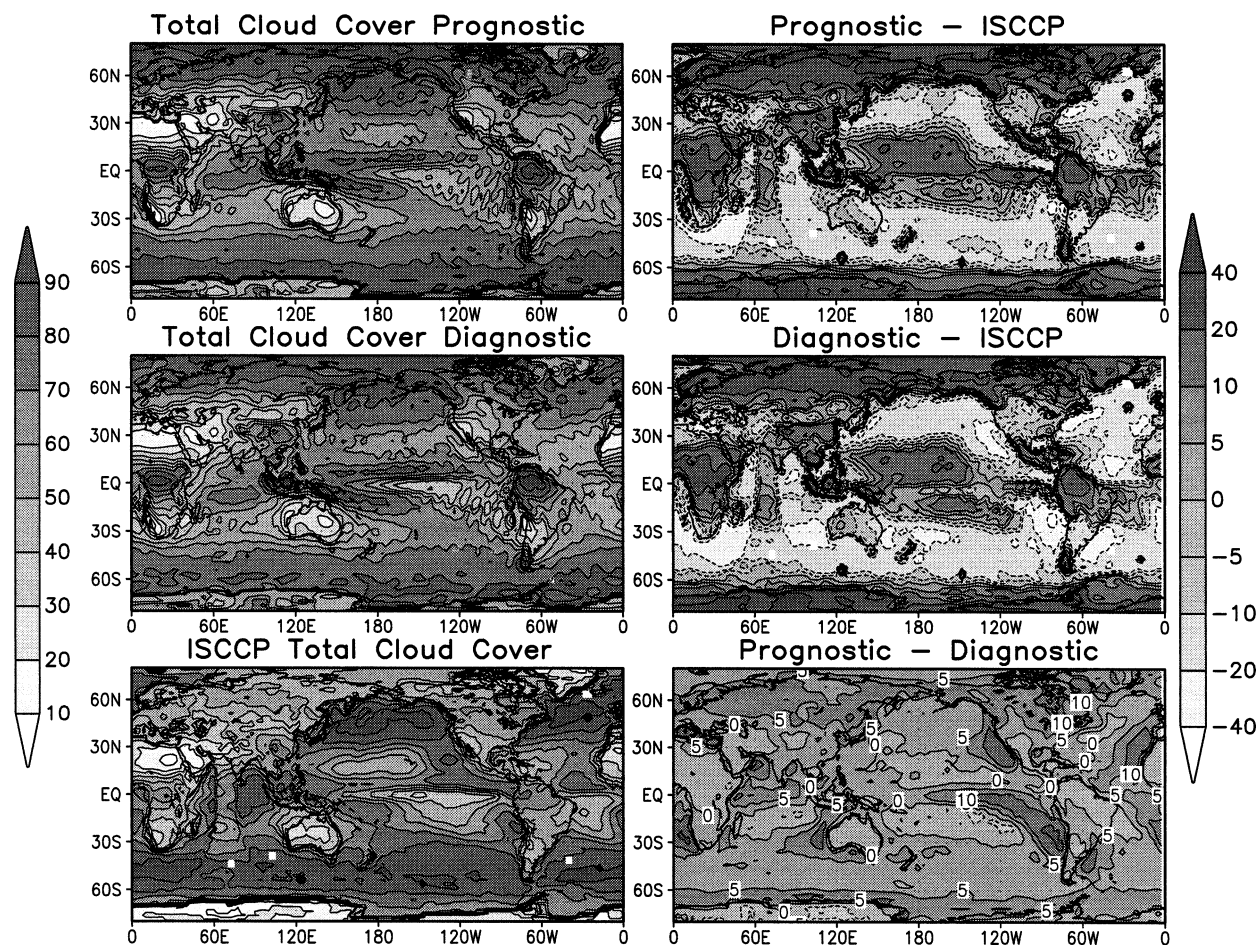
FIG. 15. (upper left) Mean total cloud cover from a 20-year T42 climate run using the new prognostic scheme, (middle left) previous RH diagnostic scheme, and (lower left) mean ISCCP total cloud cover (1983–90). (right column) The difference between the respective simulations and observations (note gray shade scale).

other physical processes, and also that the information concerning the higher-order moments can be used by other model parameterizations such as the microphysics and radiation schemes, for example. This can lead to increased consistency between model components and reduces the overall number of model "tunable" parameters.

Specifically, the following aspects will be investigated for future inclusion:

- The effect of gravity wave activity in increasing subgrid-scale variance.
- The effect of convective downdrafts on increasing lower-tropospheric negative skewness and variance.
- The consistent inclusion of subgrid-scale temperature variability.
- The relaxation of the zero supersaturation assumption for the ice phase.
- Taking into account the information related to water vapor and cloud variability in the calculation of radiative fluxes.
- Using information concerning subgrid-scale variabil-

ity of temperature and water in the PBL for the convection parameterization scheme. Thus, a grid cell with a lower mean equivalent potential temperature ($\overline{\theta_e}$) than its neighbors could still initiate convection in preference if its distribution was broader, due, perhaps, to previous convective activity.

- Taking the variability of cloud into account for microphysical processes such as precipitation generation.

Finally, we note that while improving certain aspects of cloud simulation, and offering good scope for future improvement, the present scheme does nothing to tackle other cloud modeling issues that are equally important, such as overlap assumptions (e.g., Jakob and Klein 1999; Morcrette and Jakob 2000) and vertical subgrid-scale variability. In fact, such issues become more complex if horizontal variability is taken into account.

Liquid Water Path [g/m²]
—— Prognostic — — Diagnostic ······· SSM/I
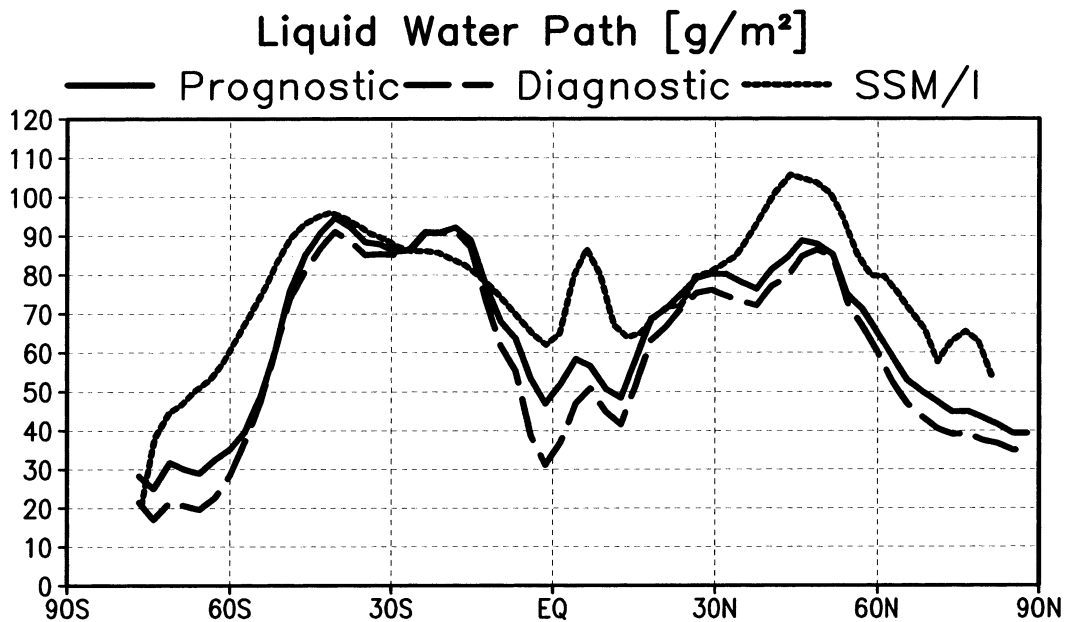
FIG. 16. Zonal mean liquid water path in GCM climate runs using new prognostic and previous diagnostic cloud scheme, compared to SSM/I retrieval (1987–91 mean).

LWCF [W/m²]
—— Prognostic — — Diagnostic ······· ERBE

FIG. 17. Zonal mean longwave cloud radiative forcing in GCM climate runs using new prognostic and previous diagnostic cloud scheme compared to ERBE-derived value (1985–88 mean).

also expresses his appreciation to ECMWF for allowing the continued collaboration with the Max Planck Institute to complete this project successfully.

APPENDIX

Description of Numerical Models

a. Cloud-resolving model

The CRM used is the Met Office large eddy simulation model, described in detail in Shutts and Gray (1994) and Tompkins and Craig (1998). The CRM includes a microphysical scheme that integrates prognostic equations for rain, snow, cloud water, cloud ice, and graupel mixing ratios, and also the ice crystal concentration number (Brown and Swann 1997). The cloud fields used in the analysis are taken from the numerical experiment of Tompkins (2001a), which used a 89.6 by 89.6 km three-dimensional domain, approximately 21 km deep. Thus this domain size is on the order of a high-resolution GCM grid box. The horizontal resolution employed in the CRM experiment was 350 m, while 50 vertical levels were used to resolve the microphysical processes (Tompkins and Emanuel 2000), with a resolution stretching from 100 m at the surface to 500 m in the upper troposphere. The experiment lasted 24 h, starting from a realistic and dynamically active cloud field, with a constant imposed radiative cooling of 2 K day^{-1} providing the forcing for convection. No large-scale convergence, vertical wind shear, or rotation was imposed.

In addition to this dataset, the distributions of r_t were also examined using the coarser resolution (2 km), large-domain (over 1000 km in length) dataset from Tompkins (2001b), in which several configurations involving vertical wind shear and large-scale sea surface temperature gradients were utilized, although the results are not reproduced in this article for reasons of brevity. It was found that these simulations also produced similar unimodal distributions, sometimes with minor cloudy secondary peaks, for which the beta distribution generally offered a good fit. The case with a strong vertical wind shear (cf. Tompkins 2001b) resulted in the poorest fit using the beta distribution.

b. General circulation model

The cloud scheme was implemented into the latest version of the Climate GCM of the Max Planck Institute for Meteorology, called ECHAM5. Previous versions of it have been successfully applied to wide variety of climate related topics (e.g., Chen and Roeckner 1997; Lohmann and Feichter 1997; Manzini et al. 1997; Bacher et al. 1998; Moron et al. 1998). The main model physics is described in detail by Roeckner et al. (1992) and Roeckner et al. (1996). The standard model uses a bulk mass-flux convective parameterization scheme based on Tiedtke (1989), containing separate representations of shallow and deep convection, modified according to Nordeng (1994) to make deep convective cloud-base mass flux a function of the convective available potential energy. Surface fluxes of heat and moisture are calculated using Monin–Obukhov similarity theory.

Additions to the new ECHAM5 code include a cloud microphysics scheme including a prognostic treatment of separate cloud ice and liquid cloud variables (Lohmann and Roeckner 1996), and the implementation of the Spitfire advection scheme (Rasch and Lawrence 1998) and a modified radiation parameterization (Mlawer et al. 1997). For the implementation experiments conducted in this paper, the standard 19-level vertical grid is used to be consistent with previous ECHAM investigations, but Tompkins and Emanuel (2000) have shown this to be inadequate to resolve all the microphysical processes, and thus future testing will be conducted at higher vertical resolutions.

c. Notes on implementation

Concerning the implementation of the new scheme, a new routine was added that was called at the beginning of each time step to diagnose cloud cover. At grid points where $r_c = 0$ or $r_v \geq r_s$, the cloud cover is set to zero or one, respectively, and the distribution minimum and maximum are calculated directly from $\overline{r}_t$, q, and $b - a$. For the other partially cloudy grid points, iteration is used to calculate a from Eq. (16), from which b and hence the width $b - a$ are simple to derive. Ridder's method was chosen (Press et al. 1992) to perform the iteration since the method is efficient, numerically very robust, and requires only the distribution limits to be known, and not the function's derivative. For computational efficiency, a lookup table was introduced for I_x with simple linear interpolation applied between table entries. The iteration is bounded by the constraints $0 < a < MIN(\overline{r}_t, r_s)$ and $b > r_s$.

Since some of the processes (e.g., microphysics) affect the distribution variance implicitly rather than explicitly, the diagnosed value for $b - a$ resulting from the iteration will sometimes differ from the current value held in the prognostic variable. This difference is added to the tendency equation for $b - a$ such that it would equal the diagnosed value after exactly one time step in the absence of other processes.

Note that unless additional precautionary measures are taken, there is nothing to prevent a combination of p, q, $\overline{r}_t$, and $\overline{r}_c$ arising that could result in negative water vapor values, that is, $a < 0$. When this occasionally occurs, an additional appropriate mass of cloud condensate is evaporated to restore the distribution to a physically valid bound ($a = 0$) over the following time step. An additional safety check at the beginning of each time step ensures that the distribution width is consistent with the values of humidity and cloud. If the distribution

width implies partially cloudy conditions, when in fact clear sky ($r_c = 0$) or overcast ($r_v = r_s$) conditions prevail, the distribution width is adjusted as necessary using the conditions $b = r_s$ or $a = r_s$, respectively.

For the variance equation, the transport of variance by vertical turbulence [second term of Eq. (20)] is solved implicitly in the model's diffusion scheme in the same way as for the other prognostic quantities. Since the vertical turbulent timescale for dissipation of variance, τ_v is much shorter than the model time step, and also because the change in variance is a small residual of large production and dissipation terms in the PBL, the other terms in Eq. 20 are also solved implicitly, [as in Tiedtke 1993, Eq. (39)], in order to avoid numerical instability problems. The timescale for the horizontal mixing term τ_h is not allowed to exceed 20 days since it is assumed that residual eddies will always be present even in cases of zero horizontal wind shear.

Although the dissipation by horizontal and vertical turbulence could in theory lead to zero variance (i.e., homogeneous distribution), in reality this limit will never be attained, due to residual gravity wave activity, for example. In practice this is in any case undesirable, since numerical inaccuracies (e.g., advection of the variance field) could lead to negative values and ensuing numerical problems. We therefore impose a small, but nonzero, lower limit to distribution width of $0.1\bar{r}_v$. Apart from the overhead of carrying an additional two prognostic equations, the scheme was found to have a 2% computational cost at T42 resolution on a scalar machine.

REFERENCES

Bacher, A., J. M. Oberhuber, and E. Roeckner, 1998: ENSO dynamics and seasonal cycle in the tropical Pacific as simulated by the ECHAM4/OPYC3 coupled general circulation model. *Climate Dyn.,* **14,** 431–450.

Barker, H. W., 1996: A parameterization for computing grid-averaged solar fluxes for inhomogeneous marine boundary layer clouds. Part I: Methodology and homogeneous biases. *J. Atmos. Sci.,* **53,** 2289–2303.

——, B. A. Wielicki, and L. Parker, 1996: A parameterization for computing grid-averaged solar fluxes for inhomogeneous marine boundary layer clouds. Part II: Validation using satellite data. *J. Atmos. Sci.,* **53,** 2304–2316.

——, G. L. Stephens, and Q. Fu, 1999: The sensitivity of domain-averaged solar fluxes to assumptions about cloud geometry. *Quart. J. Roy. Meteor. Soc.,* **125,** 2127–2152.

Bechtold, P., C. Fravalo, and J. P. Pinty, 1992: A model of marine boundary-layer cloudiness for mesoscale applications. *J. Atmos. Sci.,* **49,** 1723–1744.

——, J. W. M. Cuijpers, P. Mascart, and P. Trouilhet, 1995: Modeling of trade-wind cumuli with a low-order turbulence model—Toward a unified description of Cu and Sc clouds in meteorological models. *J. Atmos. Sci.,* **52,** 455–463.

Bergman, J. W., and H. H. Hendon, 2000: The impact of clouds on the seasonal cycle of radiative heating over the Pacific. *J. Atmos. Sci.,* **57,** 545–566.

Blackadar, A. K., 1962: The vertical distribution of wind and turbulent exchange in a neutral atmosphere. *J. Geophy. Res.,* **67,** 3095–3102.

Bougeault, P., 1981: Modeling the trade-wind cumulus boundary-layer. Part I: Testing the ensemble cloud relations against numerical data. *J. Atmos. Sci.,* **38,** 2414–2428.

——, 1982: Cloud ensemble relations based on the Gamma probability distribution for the high-order models of the planetary boundary layer. *J. Atmos. Sci.,* **39,** 2691–2700.

Bretherton, C. S., and P. K. Smolarkiewicz, 1989: Gravity waves, compensating subsidence and detrainment around cumulus clouds. *J. Atmos. Sci.,* **46,** 740–759.

Brown, P. R. A., and H. A. Swann, 1997: Evaluation of key microphysical parameters in three dimensional cloud model simulations using aircraft and multiparameter radar data. *Quart. J. Roy. Meteor. Soc.,* **123,** 2245–2275.

Brown, R, G., and C. Zhang, 1997: Variability of midtropospheric moisture and its effect on cloud-top height distribution during TOGA COARE. *J. Atmos. Sci.,* **54,** 2760–2774.

Cahalan, R. F., W. Ridgway, W. J. Wiscombe, T. L. Bell, and J. B. Snider, 1994: The albedo of fractal stratocumulus clouds. *J. Atmos. Sci.,* **51,** 2434–2455.

Cairns, B., A. A. Lacis, and B. E. Carlson, 2000: Absorption within inhomogeneous clouds and its parameterization in general circulation models. *J. Atmos. Sci.,* **57,** 700–714.

Chen, C. T., and E. Roeckner, 1997: Cloud simulations with the Max Planck Institute for Meteorology general circulation model ECHAM4 and comparison with observations. *J. Geophys. Res.,* **102,** 9335–9350.

Cusack, S., J. M. Edwards, and R. Kershaw, 1999: Estimating the subgrid variance of saturation, and its parametrization for use in a GCM cloud scheme. *Quart. J. Roy. Meteor. Soc.,* **125,** 3057–3076.

Davis, A., A. Marshak, W. Wiscombe, and R. Cahalan, 1996: Scale invariance of liquid water distributions in marine stratocumulus. Part I: Spectral properties and stationarity issues. *J. Atmos. Sci.,* **53,** 1538–1558.

Deardorff, J. W., 1974a: Three dimensional numerical study of a heated planetary boundary layer. *Bound.-Layer Meteor.,* **7,** 81–106.

——, 1974b: Three dimensional numerical study of turbulence in an entraining mixed layer. *Bound.-Layer Meteor.,* **7,** 199–226.

DelGenio, A. D., M. S. Yao, W. Kovari, and K. K. W. Lo, 1996: A prognostic cloud water parameterization for global climate models. *J. Climate,* **9,** 270–304.

Ek, M., and L. Mahrt, 1991: A formulation for boundary-layer cloud cover. *Ann. Geophys.,* **9,** 716–724.

Emanuel, K. A., and R. T. Pierrehumbert, 1996: Microphysical and dynamical control of tropospheric water vapor. *Clouds, Chemistry and Climate,* P. J. Crutzen and V. Ramanathan, Eds., Springer, 17–28.

Essenwanger, O., 1976: *Applied Statistics in Atmospheric Sciences.* Elsevier, 412 pp.

Fowler, L. D., D. A. Randall, and S. A. Rutledge, 1996: Liquid and ice cloud microphysics in the CSU general circulation model. Part I: Model description and simulated cloud microphysical processes. *J. Climate,* **9,** 489–529.

Fu, Q., B. Carlin, and G. Mace, 2000: Cirrus horizontal inhomogeneity and OLR bias. *Geophys. Res. Lett.,* **27,** 3341–3344.

Garratt, J. R., 1992: *The Atmospheric Boundary Layer.* Cambridge University Press, 316 pp.

Gates, W. L., and M. E. Schlesinger, 1977: Numerical-simulation of January and July global climate with a two-level atmospheric model. *J. Atmos. Sci.,* **34,** 36–76.

Ghan, S. J., L. R. Leung, and Q. Hu, 1997: Application of cloud microphysics to NCAR community climate model. *J. Geophys. Res.,* **102,** 16 507–16 527.

Greenwald, T. J., G. L. Stephens, T. H. Vonderhaar, and D. L. Jackson, 1993: A physical retrieval of cloud liquid water over the global oceans using special sensor microwave imager (SSM/I) observations. *J. Geophy. Res.,* **98,** 18 471–18 488.

Heymsfield, A. J., and L. M. Miloshevich, 1995: Relative humidity and temperature influences on cirrus formation and evolution:

Observations from wave clouds and FIRE II. *J. Atmos. Sci.,* **52,** 4302–4326.

——, and G. M. McFarquhar, 1996: High albedos of cirrus in the Tropical Pacific Warm Pool: Microphysical interpretations from CEPEX and from Kwajalein, Marshall Islands. *J. Atmos. Sci.,* **53,** 2424–2451.

——, R. P. Lawson, and G. W. Sachse, 1998a: Growth of ice crystals in a precipitating contrail. *Geophys. Res. Lett.,* **25,** 1335–1338.

——, L. M. Miloshevich, C. Twohy, G. Sachse, and S. Oltmans, 1998b: Upper-tropospheric relative humidity observations and implications for cirrus ice nucleation. *Geophys. Res. Lett.,* **25,** 1343–1346.

Jakob, C., and S. A. Klein, 1999: The role of vertically varying cloud fraction in the parameterization of microphysical processes in the ECMWF model. *Quart. J. Roy. Meteor. Soc.,* **125,** 941–965.

Johnson, N. L., and S. Kotz, 1970: *Continuous Univariate Distributions-2.* John Wiley and Sons, 306 pp.

Lappen, C.-L., and D. A. Randall, 2001: Toward a unified parameterization of the boundary layer and moist convection. Part I: A new type of mass-flux model. *J. Atmos. Sci.,* **58,** 2021–2036.

Larson, V. E., R. Wood, P. R. Field, J. Golaz, T. H. VonderHaar, and W. R. Cotton, 2001a: Small-scale and mesoscale variability of scalars in cloudy boundary layers: One dimensional probability density functions. *J. Atmos. Sci.,* **58,** 1978–1994.

——, ——, ——, ——, ——, and ——, 2001b: Systematic biases in the microphysics and thermodynamics of numerical models that ignore subgrid-scale variability. *J. Atmos. Sci.,* **58,** 1117–1128.

Lenderink, G., and A. P. Siebesma, 2000: Combining the massflux approach with a statistical cloud scheme. *Proc. 14th Symp. on Boundary Layers and Turbulence,* Aspen, CO, Amer. Meteor. Soc., 66–69.

LeTreut, H., and Z. X. Li, 1991: Sensitivity of an atmospheric general circulation model to prescribed SST changes: Feedback effects associated with the simulation of cloud optical properties. *Climate Dyn.,* **5,** 175–187.

Lewellen, W. S., and S. Yoh, 1993: Binormal model of ensemble partial cloudiness. *J. Atmos. Sci.,* **50,** 1228–1237.

Liao, X., and D. Rind, 1997: Local upper tropospheric/lower stratospheric clear-sky water vapor and tropospheric deep convection. *J. Geophys. Res.,* **102,** 19 543–19 557.

Lin, Y. L., R. D. Farley, and H. D. Orville, 1983: Bulk parameterization of the snow field in a cloud model. *J. Climate Appl. Meteor.,* **22,** 1065–1092.

Lohmann, U., and E. Roeckner, 1996: Design and performance of a new cloud microphysics scheme developed for the ECHAM general circulation model. *Climate Dyn.,* **12,** 557–572.

——, and J. Feichter, 1997: Impact of sulphate aerosols on albedo and lifetime of clouds. *J. Geophys. Res.,* **102,** 13 685–13 700.

——, N. McFarlane, L. Levkov, K. Abdella, and F. Albers, 1999: Comparing different cloud schemes of a single column model by using mesoscale forcing and nudging technique. *J. Climate,* **12,** 438–461.

Mannoji, N., 1995: An explicit cloud predicting scheme implemented in the Florida State University Global Spectral Model and its impact. *J. Meteor. Soc. Japan,* **73,** 993–1009.

Manzini, E., N. A. McFarlane, and C. McLandress, 1997: Impact of Doppler spread parameterization on the simulation of the middle atmosphere circulation using the MA/ECHAM4 general circulation model. *J. Geophys. Res.,* **102,** 25 751–25 762.

Mason, P. J., and N. S. Callen, 1986: On the magnitude of the subgrid-scale eddy coefficient in large-eddy simulations of turbulent channel flow. *J. Fluid Mech.,* **162,** 439–462.

——, and A. R. Brown, 1999: On subgrid models and filter operations in large eddy simulations. *J. Atmos. Sci.,* **56,** 2101–2114.

Mellor, G. L., 1977: Gaussian cloud model relations. *J. Atmos. Sci.,* **34,** 356–358.

Mlawer, E. J., S. J. Taubman, P. D. Brown, M. J. Iacono, and S. A. Clough, 1997: Radiative transfer for inhomogeneous atmo-spheres: RRTM, a validated correlated-k model for the long-wave. *J. Geophys. Res.,* **102,** 16 663–16 682.

Morcrette, J. J., and C. Jakob, 2000: The response of the ECMWF model to changes in the cloud overlap assumption. *Mon. Wea. Rev.,* **128,** 1707–1732.

Moron, V., A. Navarra, M. N. Ward, and E. Roeckner, 1998: Skill and reproducibility of seasonal rainfall patterns in the Tropics in ECHAM4 GCM simulations with prescribed SST. *Climate Dyn.,* **14,** 83–100.

Nishizawa, K., 2000: Parameterization of nonconvective condensation for low-resolution climate models: Comparison of diagnostic schemes for fractional cloud cover and cloud water content. *J. Meteor. Soc. Japan,* **78,** 1–12.

Nordeng, T. E., 1994: Extended versions of the convective parametrization scheme at ECMWF and their impact on the mean and transient activity of the model in the Tropics. ECMWF Tech. Memo 206, 41 pp. [Available from European Centre for Medium-Range Weather Forecasts, Shinfield Park, Reading RG2 9AX, United Kingdom.]

Oreopoulos, L., and H. W. Barker, 1999: Accounting for subgrid-scale cloud variability in a multi-layer 1D solar radiative transfer algorithm. *Quart. J. Roy. Meteor. Soc.,* **125,** 301–330.

Ose, T., 1993: An examination of the effects of explicit cloud water in the UCLA GCM. *J. Meteor. Soc. Japan,* **71,** 93–109.

Pierrehumbert, R. T., and H. Yang, 1993: Global chaotic mixing on isentropic surfaces. *J. Atmos. Sci.,* **50,** 2462–2480.

Pincus, R., and S. A. Klein, 2000: Unresolved spatial variability and microphysical process rates in large-scale models. *J. Geophys. Res.,* **105,** 27 059–27 065.

——, S. A. McFarlane, and S. A. Klein, 1999: Albedo bias and the horizontal variability of clouds in subtropical marine boundary layers: Observations from ships and satellites. *J. Geophys. Res.,* **104,** 6183–6191.

Pomroy, H. R., and A. J. Illingworth, 2000: Ice cloud inhomogeneity: Quantifying bias in emissivity from radar observations. *Geophys. Res. Lett.,* **27,** 2101–2104.

Press, W. H., S. A. Teukolsky, W. T. Vetterling, and B. P. Flannery, 1992: *Numerical Recipes in Fortran: The Art of Scientific Computing.* 2d ed. Cambridge University Press, 963 pp.

Price, J. D., 2001: A study on boundary layer humidity distributions and errors in parameterised cloud fraction. *Quart. J. Roy. Meteor. Soc.,* **127,** 739–759.

Ramanathan, V., R. D. Cess, E. F. Harrison, P. Minnis, B. R. Barkstrom, E. Ahmad, and D. Hartmann, 1989: Cloud-radiative forcing and climate: Results from the earth radiation budget experiment. *Science,* **243,** 57–63.

Randall, D. A., and G. J. Huffman, 1980: A stochastic model of cumulus clumping. *J. Atmos. Sci.,* **37,** 2068–2078.

Rasch, P. J., and M. Lawrence, 1998: Recent development in transport methods at NCAR. MPI workshop on conservative transport schemes, B. Machenhauer, Ed., MPI Tech. Memo. 265, 65–75. [Available from Max Planck Institute for Meteorology, Bundesstr. 55, 20146 Hamburg, Germany.]

Raymond, D. J., 2000: The Hadley circulation as a radiative–convective instability. *J. Atmos. Sci.,* **57,** 1286–1297.

Ricard, J. L., and J. F. Royer, 1993: A statistical cloud scheme for use in an AGCM. *Ann. Geophys.,* **11,** 1095–1115.

Roeckner, E., and Coauthors, 1992: Simulation of present-day climate with the ECHAM model: Impact of model physics and resolution. MPI Tech. Memo. 93, 171 pp. [Available from Max Planck Institute for Meteorology, Bundesstr. 55, 20146 Hamburg, Germany.]

——, and Coauthors, 1996: The atmospheric general circulation model ECHAM4: Model description and simulation of present-day climate. MPI Tech. Memo. 218, 90 pp. [Available from Max Planck Institute for Meteorology, Bundesstr. 55, 20146 Hamburg, Germany.]

Rossow, W. B., and R. A. Schiffer, 1991: ISCCP cloud data products. *Bull. Amer. Meteor. Soc.,* **72,** 2–20.

Rotstayn, L. D., 1997: A physically based scheme for the treatment

of stratiform precipitation in large-scale models. I: Description and evaluation of the microphysical processes. *Quart. J. Roy. Meteor. Soc.,* **123,** 1227–1282.

——, 2000: On the ''tuning'' of autoconversion parameterizations in climate models. *J. Geophys. Res.,* **105,** 15 495–15 507.

Schneider, S. H., W. M. Washington, and R. M. Chervin, 1978: Cloudiness as a climatic feedback mechanism—Effects on cloud amounts of prescribed global and regional surface-temperature changes in the NCAR-GCM. *J. Atmos. Sci.,* **35,** 2207–2221.

Sellers, W. D., 1976: A two-dimensional global climatic model. *Mon. Wea. Rev.,* **104,** 233–248.

Shutts, G. J., and M. E. B. Gray, 1994: A numerical modelling study of the geostrophic adjustment following deep convection. *Quart. J. Roy. Meteor. Soc.,* **120,** 1145–1178.

Slingo, J. M., 1980: A cloud parameterization scheme derived from GATE data for use with a numerical-model. *Quart. J. Roy. Meteor. Soc.,* **106,** 747–770.

——, 1987: The development and verification of a cloud prediction scheme for the ECMWF model. *Quart. J. Roy. Meteor. Soc.,* **113,** 899–927.

Smagorinsky, J., 1963: General circulation experiments with the primative equations. I: The basic experiment. *Mon. Wea. Rev.,* **91,** 99–164.

Smith, R. N. B., 1990: A scheme for predicting layer clouds and their water-content in a general-circulation model. *Quart. J. Roy. Meteor. Soc.,* **116,** 435–460.

Sommeria, G., 1976: Three-dimensional simulation of turbulent processes in an undisturbed trade wind boundary layer. *J. Atmos. Sci.,* **33,** 216–241.

——, and J. W. Deardorff, 1977: Subgrid-scale condensation in models of nonprecipitating clouds. *J. Atmos. Sci.,* **34,** 344–355.

Stull, R. B., 1988: *An Introduction to Boundary Layer Meteorology.* Kluwer Academic, 666 pp.

Sundqvist, H., 1978: A parameterization scheme for non-convective condensation including prediction of cloud water content. *Quart. J. Roy. Meteor. Soc.,* **104,** 677–690.

——, E. Berge, and J. E. Kristjansson, 1989: Condensation and cloud parameterization studies with a mesoscale numerical weather prediction model. *Mon. Wea. Rev.,* **117,** 1641–1657.

Tiedtke, M., 1989: A comprehensive mass flux scheme for cumulus parameterization in large-scale models. *Mon. Wea. Rev.,* **117,** 1779–1800.

——, 1993: Representation of clouds in large-scale models. *Mon. Wea. Rev.,* **121,** 3040–3061.

——, 1996: An extension of cloud-radiation parameterization in the ECMWF model: The representation of subgrid-scale variations of optical depth. *Mon. Wea. Rev.,* **124,** 745–750.

Tompkins, A. M., 2001a: Organization of tropical convection in low vertical wind shears: The role of coldpools. *J. Atmos. Sci.,* **58,** 1650–1672.

——, 2001b: Organization of tropical convection in low vertical wind shears: The role of water vapor. *J. Atmos. Sci.,* **58,** 529–545.

——, and G. C. Craig, 1998: Radiative-convective equilibrium in a three-dimensional cloud ensemble model. *Quart. J. Roy. Meteor. Soc.,* **124,** 2073–2097.

——, and K. A. Emanuel, 2000: The vertical resolution sensitivity of simulated equilibrium temperature and water vapour profiles. *Quart. J. Roy. Meteor. Soc.,* **126,** 1219–1238.

Walcek, C. J., 1994: Cloud cover and its relationship to relative-humidity during a springtime midlatitude cyclone. *Mon. Wea. Rev.,* **122,** 1021–1035.

Wang, S., and Q. Wang, 1999: On condensation and evaporation in turbulence cloud parameterizations. *J. Atmos. Sci.,* **56,** 3338–3344.

Wielicki, B. A., and L. Parker, 1994: Frequency distributions of cloud liquid water path in oceanic boundary layer cloud as a function of regional cloud fraction. *Proc. Eighth Conf. on Atmospheric Radiation,* Nashville, TN, Amer. Meteor. Soc., 415–417.

Wood, R., and P. R. Field, 2000: Relationship between total water, condensed water, and cloud fraction in stratiform clouds examined using aircraft data. *J. Atmos. Sci.,* **57,** 1888–1905.

Xu, K.-M., and S. K. Krueger, 1991: Evaluation of cloudiness parameterizations using a cumulus ensemble model. *Mon. Wea. Rev.,* **119,** 342–367.

——, and D. A. Randall, 1996a: A semiempirical cloudiness parameterization for use in climate models. *J. Atmos. Sci.,* **53,** 3084–3102.

——, and ——, 1996b: Evaluation of statistically based cloudiness parameterizations used in climate models. *J. Atmos. Sci.,* **53,** 3103–3119.